PHYSICAL REVIEW D **95,** 075035 (2017)

Can we probe intrinsic *CP* and *T* violations and nonunitarity at long baseline accelerator experiments?

Jogesh Rout,[1,*] Mehedi Masud,[2,3,†] and Poonam Mehta[1,‡]

[1]*School of Physical Sciences, Jawaharlal Nehru University, New Delhi 110067, India*
[2]*Astroparticle and High Energy Physics Group, Institut de Física Corpuscular—C.S.I.C./Universitat de València, Parc Cientific de Paterna, C/Catedratico José Beltrán, 2 E-46980 Paterna (València), Spain*
[3]*Harish-Chandra Research Institute, Chhatnag Road, Jhunsi, Allahabad 211 019, India*

(Received 15 February 2017; published 25 April 2017)

One of the fundamental parameters entering the neutrino oscillation framework is the leptonic *CP* phase δ_{13}, and its measurement is an important goal of the planned long baseline experiments. It should be noted that ordinary matter effects complicate the determination of this parameter, and there are studies in the literature that deal with separation of intrinsic vs extrinsic *CP* violation. It is important to investigate the consequences of new physics effects that can not only hamper the measurement of δ_{13} but also impact the consequences of discrete symmetries such as *CP*, *T*, and unitarity in different oscillation channels. In the present work, we explore these discrete symmetries and implications on unitarity in the presence of two new physics scenarios (nonstandard interaction in propagation and the presence of sterile neutrinos) that serve as good examples of going beyond the standard scenario in different directions. We uncover the impact of new physics scenarios on disentangling intrinsic and extrinsic *CP* violation.

DOI: 10.1103/PhysRevD.95.075035

I. INTRODUCTION

The possibility of neutrino oscillations was first raised in a seminal paper by Pontecorvo [1], and almost 60 years later, the experimental confirmation of neutrino oscillations was rewarded with a Nobel Prize [2]. The standard three-flavor neutrino mixing parameters are three angles (θ_{12}, θ_{13}, θ_{23}), two mass splittings ($\delta m^2_{31}, \delta m^2_{21}$), and one phase ($\delta_{13}$) that is responsible for *CP* violation in the leptonic sector. While the mixing angles and the mass-squared differences (and absolute value of only one of them) have been measured with varying degrees of precision (see Table I), the measured value of θ_{13} allows for an early measurement of the leptonic *CP* violation [3–5].

The three-flavor neutrino mixing matrix $\mathcal{U}$ is parametrized by three angles, θ_{12}, θ_{23}, and θ_{13} and one phase δ_{13}.[1] In the Pontecorvo-Maki-Nakagawa-Sakata parametrization [6], $\mathcal{U}$ is given by

$$\mathcal{U} = \begin{pmatrix} c_{12}c_{13} & s_{12}c_{13} & s_{13}e^{-i\delta_{13}} \\ -s_{12}c_{23} - c_{12}s_{13}s_{23}e^{i\delta_{13}} & c_{12}c_{23} - s_{12}s_{13}s_{23}e^{i\delta_{13}} & c_{13}s_{23} \\ s_{12}s_{23} - c_{12}s_{13}c_{23}e^{i\delta_{13}} & -c_{12}s_{23} - s_{12}s_{13}c_{23}e^{i\delta_{13}} & c_{13}c_{23} \end{pmatrix}, \tag{1}$$

where $s_{ij} = \sin\theta_{ij}, c_{ij} = \cos\theta_{ij}$. The validity of the three-flavor neutrino paradigm relies very heavily on the assumption of 3×3 unitarity of the mixing matrix. Most of the information about the parameters of the neutrino mixing matrix is gleaned from a vast variety of experiments. We should realize that much of the information originates from ν_μ and ν_e sector via disappearance ($\bar{\nu}_e \to \bar{\nu}_e$ in the case of reactor experiments and $\bar{\nu}_\mu \to \bar{\nu}_\mu$ in the case of atmospheric and long baseline experiments) and appearance ($\nu_\mu \to \nu_e$) measurements in the ongoing and future long baseline neutrino oscillation experiments. The remaining elements in the mixing matrix are fixed assuming unitarity, i.e., probability conservation [7]. Clearly, data from neutrino experiments are not sufficient to constrain all the elements of the leptonic mixing matrix [8]. On the other hand, the assumption of unitarity in the quark sector is justified well by data.

Within the Standard Model (SM), the *CP* symmetry is broken by complex phases in the Yukawa couplings. After removing the unphysical phases in the SM, there is only one physical phase which is the *CP*-violating parameter.

*jogesh.rout1@gmail.com
†masud@ific.uv.es
‡pm@jnu.ac.in

[1]For n flavors, the leptonic mixing matrix $U_{\alpha i}$ depends on $(n-1)(n-2)/2$ Dirac-type *CP*-violating phases. If the neutrinos are Majorana particles, there are $(n-1)$ additional so-called Majorana-type *CP*-violating phases.

TABLE I. The best-fit values, 3σ ranges, and precision (in a percentage) of the six parameters from the latest global fit to neutrino data [5]. For entries with two rows, the first (second) row corresponds to Normal hierarchy (NH) (Inverted hierarchy, IH). For NH, $\delta m^2_{3l} \equiv \delta m^2_{31} > 0$, and for IH, $\delta m^2_{3l} \equiv \delta m^2_{32} < 0$. Asterisks denote undetermined.

Parameter	Best-fit value	3σ range	Precision (%)
$\sin^2\theta_{12}$	0.304	$0.270 \to 0.344$	12
$\sin^2\theta_{13}$	0.0218	$0.0186 \to 0.0250$	14
	0.0219	$0.0188 \to 0.0251$	14
$\sin^2\theta_{23}$	0.452	$0.382 \to 0.643$	25
	0.579	$0.389 \to 0.644$	24
δm^2_{21} [10^{-5} eV^2]	7.50	$7.02 \to 8.09$	
δm^2_{3l} [10^{-3} eV^2]	$+2.457$	$7 + 2.317 \to +2.607$	6
	-2.449	$-2.590 \to -2.307$	6
δ_{13}	*	$[-\pi : \pi]$	*

This economical description of CP violation in the SM is referred to as the Kobayashi-Maskawa (KM) mechanism [9]. But if neutrinos are Majorana particles, there can be two additional Majorana-type phases in the three-flavor case which cannot be probed via oscillation experiments. In vacuum, the lone CP phase given by the KM mechanism accounts for the CP-violation signal. However, standard interaction (SI) along with the inherent CP asymmetry present in the Earth matter introduces effects that mimic CP violation. These are referred to as fake/extrinsic CP-violating effects as opposed to the genuine/intrinsic CP-violating effect due to the presence of δ_{13} [10–15]. Earlier attempts have proposed experimental arrangements [16] and observables useful in disentangling the intrinsic and extrinsic CP-violation components [15]; however, standard physics has been assumed. Our work differs in the fact that we analyze this question in the backdrop of three distinct physics scenarios (SI and two possible subdominant new physics effects) and quantitatively demonstrate that new physics further hinders clean extraction of the intrinsic component. We also quantify our results in terms of event rates and make realistic inferences about separability between the intrinsic and extrinsic CP-violating effects.

In the era of precision measurements in neutrino oscillation physics, we need to consider subdominant new physics scenarios such as nonstandard neutrino interactions (NSI) or sterile neutrinos and discuss the capabilities of our planned experiments for some benchmark values of new physics parameters. We study how neutrino oscillations have the potential to shed light on these crucial questions relating CP and T symmetries as well as the unitarity of the neutrino mixing matrix. We also probe deviations due to new physics scenarios. We go beyond the SM in two respects, one in which we introduce subdominant effects due to a possible source of new physics dubbed as NSI [17–26] and another where the presence of an extra sterile state can lead to nonunitarity in the 3×3 part even though the overall mixing matrix is still unitary [27–34], and examine consequences relevant to long baseline experiments (for other new physics scenarios such as nonunitarity, see Refs. [35–39]). We highlight the regions in $L - E$ space where the effects due to CP and T violation are drastically modified due to new physics. Our discussion is mostly targeted toward accelerator-based neutrino experiments with $L/E \sim 500$ km/GeV but can easily be extended to short baseline experiments and very long baseline experiments.

The plan of the article is as follows. In Sec. II A, we give general definitions of CP, T, and CPT asymmetries and the unitarity condition. In Sec. II B, we give the three-flavor framework in vacuum (Sec. II B 1) and in NSI along with the choice of NSI parameters (Sec. II B 2). In Sec. II C, we describe the framework and choice of parameters for the sterile neutrino case. Our results are discussed in Sec. III. The CP and T asymmetries are described for the three physics scenarios as a function of E and L in Sec. III A. For a test of nonunitarity in the sterile neutrino case, we use oscillograms as our main tool (see Sec. III B). In Sec. III C, we discuss the spectral differences in oscillogram patterns for the three physics scenarios considered.[2] Finally, we discuss prospects of CP violation and implications of our studies for long baseline experiments with particular emphasis on T2K, T2HK, NOvA, and DUNE in Sec. IV. We conclude in Sec. V.

II. FRAMEWORK

A. CP, T, and CPT asymmetries and unitarity condition: Definitions and general remarks

C, P, and T are discrete symmetries that refer to charge conjugation, parity, and time reversal, respectively. CP, T and CPT violation signal in any neutrino oscillation experiment is characterised via a comparison of probability for a given pair of initial and final flavors $\nu_\alpha \to \nu_\beta$ with their CP, T or CPT conjugate counterparts

$$\begin{aligned} CP&: \nu_{\alpha,\beta} \Rightarrow \bar{\nu}_{\alpha,\beta} \\ T&: \nu_{\alpha,\beta} \Rightarrow \nu_{\beta,\alpha} \\ CPT&: \nu_{\alpha,\beta} \Rightarrow \bar{\nu}_{\beta,\alpha}. \end{aligned} \tag{2}$$

The action of CP and T are equivalent to complex conjugation of $U_{\alpha i}$. For theoretical discussions on CP, T, and CPT in neutrino oscillations; see Refs. [40–44]. There can be no CP violation in the two-flavor case in vacuum as the unitary matrix in the two-flavor case can always be made real. In matter with varying density, this

[2]For simplicity, we assume CP-conserving new physics scenarios (i.e., all NSI and sterile neutrino phases are set to zero) while obtaining the oscillograms.

need not be the case (for geometric visualization, see Refs. [45,46]). Some theoretical consequences of the value of the CP-violating phase were discussed in Ref. [47]. The cosmological effect of CP violation was discussed in Ref. [48].

Let us define the asymmetries[3]

$$A^{CP}_{\alpha\beta} = \frac{P_{\alpha\beta} - \bar{P}_{\alpha\beta}}{P_{\alpha\beta} + \bar{P}_{\alpha\beta}} = \frac{\Delta P^{CP}_{\alpha\beta}}{\sum P^{CP}_{\alpha\beta}}, \tag{3}$$

$$A^{T}_{\alpha\beta} = \frac{P_{\alpha\beta} - P_{\beta\alpha}}{P_{\alpha\beta} + P_{\beta\alpha}} = \frac{\Delta P^{T}_{\alpha\beta}}{\sum P^{T}_{\alpha\beta}}, \tag{4}$$

$$A^{CPT}_{\alpha\beta} = \frac{P_{\alpha\beta} - \bar{P}_{\beta\alpha}}{P_{\alpha\beta} + \bar{P}_{\beta\alpha}} = \frac{\Delta P^{CPT}_{\alpha\beta}}{\sum P^{CPT}_{\alpha\beta}}, \tag{5}$$

which involve both neutrinos and antineutrinos and in which $P_{\alpha\beta}$ is the probability for transition $\nu_\alpha \to \nu_\beta$ and $\bar{P}_{\alpha\beta}$ is the probability for transition $\bar{\nu}_\alpha \to \bar{\nu}_\beta$. The probability expression is given by

$$P_{\alpha\beta} = \sum_{i,j} U_{\alpha i} U^{\star}_{\beta i} U^{\star}_{\alpha j} U_{\beta j} \exp\left\{-i \frac{\delta m^2_{ij} L}{2E}\right\}. \tag{6}$$

Obviously, these asymmetries present themselves in different channels (appearance and disappearance) that can be employed to study CP, T, and CPT violation. If CP were exact, the laws of nature would be the same for matter and antimatter. While most phenomena are CP symmetric, weak interactions violate C and P in the strongest possible way. T violation is expected as a corollary of CP violation if the combined CPT transformation is a fundamental symmetry of nature.

For three-flavor case, there are $9+9$ appearance and disappearance probability channels for neutrinos and antineutrinos. Further, the unitarity of the 3×3 mixing matrix (excluding the case of the additional sterile neutrino)

$$\sum_i U_{\alpha i} U^{*}_{\beta i} = \delta_{\alpha\beta} \tag{7}$$

can be translated in terms of probability conservation conditions

$$\sum_\beta P_{\alpha\beta} = \sum_\alpha P_{\alpha\beta} = 1, \tag{8}$$

$$\sum_\beta \bar{P}_{\alpha\beta} = \sum_\alpha \bar{P}_{\alpha\beta} = 1, \tag{9}$$

which are $6+6$ conditions, of which $5+5$ are independent. This tells us that $4(=9-5)+4$ neutrino and antineutrino oscillation probabilities are independent. Further, it may be possible to reduce the number of independent channels to just two for neutrino (and two for antineutrino) oscillation probabilities in case of SI. In the parametrization considered [Eq. (1)], the 23 rotation matrix commutes with the matter part in the Hamiltonian. Denoting the θ_{23} transformed probabilities by

$$\tilde{P}_{\alpha\beta} \equiv P_{\alpha\beta}(s^2_{23} \leftrightarrow c^2_{23}, \sin 2\theta_{23} \to -\sin 2\theta_{23}), \alpha,\beta = e,\mu,\tau, \tag{10}$$

we can show that

$$P_{e\tau} = \tilde{P}_{e\mu}, \qquad P_{\tau\mu} = \tilde{P}_{\mu\tau} \quad \text{and} \quad P_{\tau\tau} = \tilde{P}_{\mu\mu}, \tag{11}$$

and P_{ee} turns out to be independent of θ_{23}. Due to unitarity, only two of these are independent [40]. Moreover, since the antineutrino probabilities are related to neutrino probabilities by $\delta_{13} \to -\delta_{13}$ and $A \to -A$, we are left with just two independent probabilities (one possible choice could be $P_{e\mu}$ and $P_{\mu\tau}$).[4]

The unitarity condition leads to the following conditions involving CP asymmetries since $\sum_\beta (P_{\alpha\beta} - \bar{P}_{\alpha\beta}) = 0$ and $\sum_\alpha (P_{\alpha\beta} - \bar{P}_{\alpha\beta}) = 0$:

$$\begin{aligned}
\Delta P^{CP}_{ee} + \Delta P^{CP}_{e\mu} + \Delta P^{CP}_{e\tau} &= 0,\\
\Delta P^{CP}_{\mu e} + \Delta P^{CP}_{\mu\mu} + \Delta P^{CP}_{\mu\tau} &= 0,\\
\Delta P^{CP}_{\tau e} + \Delta P^{CP}_{\tau\mu} + \Delta P^{CP}_{\tau\tau} &= 0,\\
\Delta P^{CP}_{ee} + \Delta P^{CP}_{\mu e} + \Delta P^{CP}_{\tau e} &= 0,\\
\Delta P^{CP}_{e\mu} + \Delta P^{CP}_{\mu\mu} + \Delta P^{CP}_{\tau\mu} &= 0,\\
\Delta P^{CP}_{e\tau} + \Delta P^{CP}_{\mu\tau} + \Delta P^{CP}_{\tau\tau} &= 0.
\end{aligned} \tag{12}$$

Similarly, in terms of T asymmetries, since $\sum_\beta (P_{\alpha\beta} - P_{\beta\alpha}) = 0$ and $\sum_\alpha (P_{\alpha\beta} - P_{\beta\alpha}) = 0$,

$$\begin{aligned}
\Delta P^{T}_{ee} + \Delta P^{T}_{e\mu} + \Delta P^{T}_{e\tau} &= 0\\
\Delta P^{T}_{\mu e} + \Delta P^{T}_{\mu\mu} + \Delta P^{T}_{\mu\tau} &= 0\\
\Delta P^{T}_{\tau e} + \Delta P^{T}_{\tau\mu} + \Delta P^{T}_{\tau\tau} &= 0\\
\Delta P^{T}_{ee} + \Delta P^{T}_{\mu e} + \Delta P^{T}_{\tau e} &= 0\\
\Delta P^{T}_{e\mu} + \Delta P^{T}_{\mu\mu} + \Delta P^{T}_{\tau\mu} &= 0\\
\Delta P^{T}_{e\tau} + \Delta P^{T}_{\mu\tau} + \Delta P^{T}_{\tau\tau} &= 0.
\end{aligned} \tag{13}$$

[3]The denominator $\sum P_{\alpha\beta}(\delta_{13})$ has the effect of rescaling the asymmetry curves.

[4]The choice of these independent probabilities should be such that they should have θ_{23} dependence and the pair should not be connected by time reversal.

B. Three active neutrinos only

As is well known, the three neutrino flavor states can be mapped to a three-level quantum system with distinct energy eigenvalues, $E_i = p + m_i^2/2p$, in the ultrarelativistic limit in vacuum along with the assumption of equal fixed momenta (or energy). In the presence of matter, the relativistic dispersion relation $E_i = f(p, m_i)$ gets modified due to the neutrino matter interactions during propagation.

1. Propagation in vacuum

The effective Hamiltonian is given by

$$\mathcal{H}_{\rm v} = \lambda \left\{ \mathcal{U} \begin{pmatrix} 0 & & \\ & r_\lambda & \\ & & 1 \end{pmatrix} \mathcal{U}^\dagger \right\}, \tag{14}$$

where

$$\lambda \equiv \frac{\delta m^2_{31}}{2E}; \qquad r_\lambda \equiv \frac{\delta m^2_{21}}{\delta m^2_{31}}. \tag{15}$$

We first briefly review the case of CPT conservation, i.e., $A^{CPT}_{\alpha\beta} = 0$, which immediately relates CP and T asymmetries as

$$A^{CP}_{\alpha\beta} = -A^{CP}_{\beta\alpha} = A^{T}_{\alpha\beta} = -A^{T}_{\beta\alpha} \quad \text{and} \quad A^{CP}_{\alpha\alpha} = 0 = A^{T}_{\alpha\alpha}. \tag{16}$$

Because of this, the CP asymmetry vanishes when $\alpha = \beta$ (disappearance channels). Further, if we assume unitarity of the mixing matrix, the CP and T asymmetries in the appearance channels are equal to one another in vacuum,

$$\begin{aligned} & A^{CP}_{e\mu} = A^{CP}_{\mu\tau} = A^{CP}_{\tau e} = A^{T}_{e\mu} = A^{T}_{\mu\tau} = A^{T}_{\tau e} \\ \Rightarrow\ & \Delta P^{CP}_{\alpha\beta} = \Delta P^{T}_{\alpha\beta} = \Delta P, \end{aligned} \tag{17}$$

where the probability difference in the appearance channels responsible for CP (T) violation is given by ΔP. Now, in vacuum, we showed that Eq. (17) holds, which means that the CP- and T-violating probability differences in the appearance channels are equal to one another. The numerator in the CP asymmetry [defined in Eq. (3)] is given by

$$\begin{aligned} \Delta P^{CP}_{\alpha\beta} &= 8J \left[\sin(r_\lambda \lambda L) \sin^2 \frac{\lambda L}{2} - \sin(\lambda L) \sin^2 \frac{r_\lambda \lambda L}{2} \right] \\ &= 4 \sin\delta_{13} J_r [\sin \lambda L/2 \sin r_\lambda \lambda L/2 \sin (1 - r_\lambda) \lambda L/2], \end{aligned} \tag{18}$$

where $J = s_{12}c_{12}s_{23}c_{23}s_{13}c^2_{13} \sin\delta_{13}$ is the Jarlskog invariant and $J_r = J/\sin\delta_{13}$. The second line is obtained after rearranging the terms in the first line. To have observable effects, we should have sizeable interference terms that involve the CP-violating phase δ. This implies that both $\lambda L/2$ as well as $r_\lambda \lambda L/2$ must be taken into account. Naturally, the $A^{CP}_{\alpha\beta}(\delta_{13})$ vanishes as $\delta_{13} \to 0, \pi$ and when $\delta_{13} = \pm\pi/2$, $A^{CP}_{\alpha\beta}(\delta_{13})$ attains maximal values. Also, it can be noted that the normalized $A^{CP}_{\alpha\beta}(\delta_{13})$ grows linearly with L/E.

Since the three CP-/T-odd probability differences (involving different channels) are equal to one another, it suffices to look for CP violation in only one of the three possible channels (say, $\nu_\mu \to \nu_e$), and the conclusions drawn (i.e., whether CP/T is conserved or violated) can be safely extended to include the remaining channels which may be difficult to explore otherwise (for example, $\nu_\mu \to \nu_\tau$. etc). Therefore, CP conservation or violation in the case of vacuum can be established by looking at any one of the asymmetries.

2. Propagation in matter with effects due to NSI switched on

The effective Hamiltonian in the flavor basis entering the Schrödinger equation for neutrino propagation is given by

$$\begin{aligned} \mathcal{H}_{\rm f} &= \mathcal{H}_{\rm v} + \mathcal{H}_{\rm SI} + \mathcal{H}_{\rm NSI} \\ &= \lambda \left\{ \mathcal{U} \begin{pmatrix} 0 & & \\ & r_\lambda & \\ & & 1 \end{pmatrix} \mathcal{U}^\dagger + r_A \begin{pmatrix} 1 & 0 & 0 \\ 0 & 0 & 0 \\ 0 & 0 & 0 \end{pmatrix} \right. \\ &\quad \left. + r_A \begin{pmatrix} \varepsilon_{ee} & \varepsilon_{e\mu} & \varepsilon_{e\tau} \\ \varepsilon_{e\mu}^\star & \varepsilon_{\mu\mu} & \varepsilon_{\mu\tau} \\ \varepsilon_{e\tau}^\star & \varepsilon_{\mu\tau}^\star & \varepsilon_{\tau\tau} \end{pmatrix} \right\}, \end{aligned} \tag{19}$$

where

$$r_A \equiv \frac{A(x)}{\delta m^2_{31}} \tag{20}$$

and $A(x) = 2\sqrt{2} E G_F n_e(x)$, where n_e is the electron number density.

The three terms in Eq. (19) are due to vacuum, matter with SI, and matter with NSI, respectively. For the NSI case, the $\varepsilon_{\alpha\beta} (\equiv |\varepsilon_{\alpha\beta}| e^{i\varphi_{\alpha\beta}})$ are complex parameters which appear in $\mathcal{H}_{NSI}$. As a result of the Hermiticity of the Hamiltonian, we have nine additional parameters (three phases and six amplitudes appearing $\mathcal{H}_{NSI}$).

Switching on matter effects destroys the nice feature of the equality of CP and T asymmetries in case of vacuum [see Eq. (15)] due to the fact that matter effects can fake the CP-violation signal. In such a scenario, establishing CP conservation/violation in a particular channel is not enough to conclude overall CP/T violation in the leptonic sector in general, and one needs to examine asymmetries in all

possible channels. Even if it were the case, one would need to determine whether the source of *CP* violation is genuine or fake (depending on the baseline) [49]. In presence of NSI, this is further disturbed due to the presence of additional parameters (see Refs. [17,20,21]). On top of that, in the case of NSI, there are new genuine sources of *CP* violation as well as new fake sources of *CP* violation (also known as matter effects) that can change the asymmetries even further. For models with possibilities of large NSI, see Refs. [50–53].

C. Three active and one sterile neutrino

This case corresponds to a four-level quantum system with the 4×4 unitary matrix given by

$$\mathcal{U}^{\text{sterile}} = \mathcal{O}_{34}\mathcal{O}_{24}\mathcal{O}_{14}\mathcal{O}_{23}\mathcal{O}_{13}\mathcal{O}_{12}$$

$$\mathcal{O}_{24} = \begin{pmatrix} 1 & 0 & 0 & 0 \\ 0 & c_{24} & 0 & e^{-i\delta_{24}}s_{24} \\ 0 & 0 & 1 & 0 \\ 0 & -e^{i\delta_{24}}c_{24} & 0 & c_{24} \end{pmatrix};$$

$$\mathcal{O}_{14} = \begin{pmatrix} c_{14} & 0 & 0 & s_{14} \\ 0 & 1 & 0 & 0 \\ 0 & 0 & 1 & 0 \\ -s_{14} & 0 & 0 & c_{14} \end{pmatrix}. \tag{21}$$

In general, $\mathcal{O}_{ij}$ is a rotation matrix in the $i-j$ plane parametrized by angle θ_{ij} and phase δ_{ij}.

In the presence of an additional sterile neutrino, the conditions

$$\sum_{\beta} P_{\alpha\beta} = 1 = \sum_{\beta} \bar{P}_{\alpha\beta} \tag{22}$$

are valid if β takes values e, μ, τ, s (s stands for sterile). The unitarity condition leads to the conditions involving *CP* asymmetries since $\sum_{\beta}(P_{\alpha\beta} - \bar{P}_{\alpha\beta}) = 0$,

$$\begin{aligned} \sum_{\alpha=e,\mu,\tau} \Delta P^{CP}_{e\alpha} + \Delta P^{CP}_{es} &= 0 \\ \sum_{\alpha=e,\mu,\tau} \Delta P^{CP}_{\mu\alpha} + \Delta P^{CP}_{\mu s} &= 0 \\ \sum_{\alpha=e,\mu,\tau} \Delta P^{CP}_{\tau\alpha} + \Delta P^{CP}_{\tau s} &= 0 \\ \sum_{\alpha=e,\mu,\tau} \Delta P^{CP}_{s\alpha} + \Delta P^{CP}_{ss} &= 0, \end{aligned} \tag{23}$$

and $\sum_{\alpha}(P_{\alpha\beta} - \bar{P}_{\alpha\beta}) = 0$ would give four more conditions. Similarly, we can get conditions in terms of *T* asymmetries as $\sum_{\beta}(P_{\alpha\beta} - P_{\beta\alpha}) = 0$ and $\sum_{\alpha}(P_{\alpha\beta} - P_{\beta\alpha}) = 0$. Since we can only detect the active flavors, the presence of sterile neutrinos can be felt via the flavor-dependent measure of nonunitarity.

The choice of parameters used is given in Table III.

III. RESULTS AND DISCUSSION

A. *CP* and *T* asymmetries as a function of *E* and *L*

The *CP* asymmetries in three appearance channels are plotted as a function of E and L in Figs. 1 and 2 for a fixed baseline of $L = 1300$ km and a fixed energy of $E = 1$ GeV, respectively. Also, the *T* asymmetries are plotted in Figs. 3 and 4. In all the figures, the three rows correspond to the three different channels, while the three columns correspond to the cases of SI, NSI, and sterile neutrinos. The solid line refers to the case in which all *CP*-violating phases including δ_{13} are set to zero. The dotted (dashed) lines refer to $\delta_{13} = \pi/2 (\delta_{13} = -\pi/2)$ and all additional phases set to zero. The gray bands correspond to the variation in phases of additional parameters in the presence of new physics (see the previous section). We can infer the following from these plots:

(i) *CP asymmetry.*—One would expect the *CP* asymmetry to vanish when $\delta_{13} = 0$ in vacuum [see Eq. (18)]. From Figs. 1 and 2, we note that in all the three physics scenarios we get nontrivial effects. The size of the effect depends upon the channel and the choice of parameters considered. For example, for a fixed baseline of 1300 km as considered in Fig. 1 and the $\nu_\mu \to \nu_e$ channel, we notice that for $\delta_{13} = 0$ there is a nontrivial effect due to matter even in the case of SI which is prominent near lower energies (around 4%–8% near the peak). The magnitude is similar in the cases of NSI and sterile neutrino near the peak. However, there are spectral differences in the three cases which may or may not be visible depending on the particular channel.

In Fig. 2, we plot the *CP* asymmetry as a function of L for a fixed value of $E = 1$ GeV. The three curves (solid, dashed, and dotted) are oscillatory in nature, and we note that there exist specific values of baselines for which one cannot distinguish the curves for the cases $\delta_{13} = \pm\pi/2$ and $\delta_{13} = 0$. These lie near 1000 and 2000 km. In $\Delta P^{CP}_{\mu\tau}$, we note that surprisingly all three curves meet near these values of the baseline.

Here, again, for $\delta_{13} = 0$, there is a nontrivial effect due to Earth matter and the size of the effect increases with baseline and prominently for the new physics scenarios. The spectral differences are also visible here.

(ii) *T asymmetry.*—We note that $\delta_{13} = 0$ (solid line in Fig. 3) leads to vanishing asymmetry in all three cases (SI, NSI, and sterile neutrinos). Also, the dotted and dashed lines are similar in all three physics cases except for the $e-\tau$ channel in the

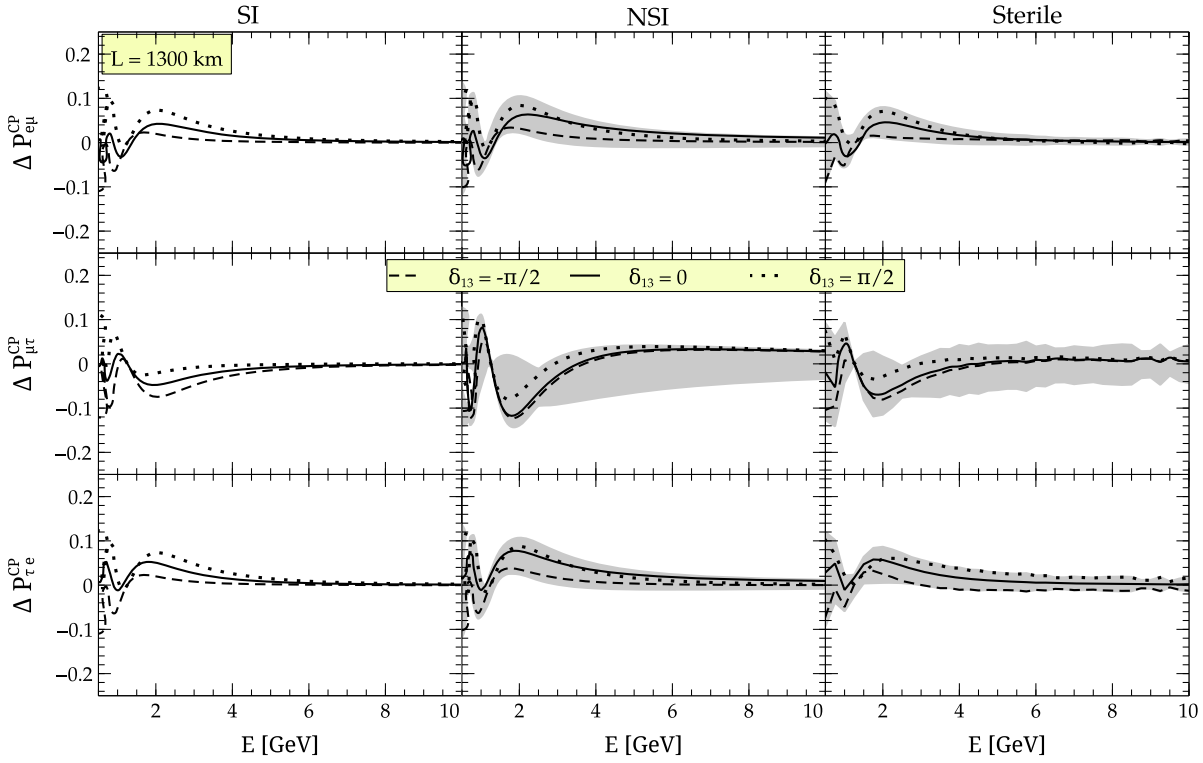

FIG. 1. CP-odd probability difference ($\Delta P^{CP}_{\alpha\beta}$) plotted as a function of energy at a fixed baseline of $L = 1300$ km. The three rows correspond to the different channels considered, while the three columns refer to effects due to SI, NSI, and sterile neutrinos. The solid line corresponds to the case in which all CP-violating phases are set to zero including δ_{13}. The dotted (dashed) line corresponds to the case in which $\delta_{13} = \pi/2(\delta_{13} = -\pi/2)$ and all additional phases are set to zero. The gray bands in the cases of NSI and sterile neutrinos refer to the variation in phases of the additional parameters introduced in their allowed ranges along with the SI phase δ_{13} (see Tables I, II, and III for the values of the parameters used).

sterile neutrino case. Of course, if additional phases are present, there are nontrivial spectral differences which can be seen as gray bands.

In Fig. 4, we plot the T asymmetry as a function of L for a fixed value of $E = 1$ GeV. The three curves (solid, dashed, and dotted) are oscillatory in nature, and we note that at specific values (or range of values) of baselines the three cases ($\delta_{13} = \pm\pi/2,\ \delta_{13} = 0$) are indistinguishable. The spectral differences are also visible more prominently in the sterile neutrino case.

B. Test of unitarity violation: Oscillograms

We use colored oscillograms in the plane of E and L as our tool to depict our observations. For the case of SI and neutral current NSI, the three-flavor unitarity is maintained, and therefore if we plot the sum of CP-odd probability differences, we expect to get blank regions in these cases. However, for the case of one additional sterile neutrino, we obtain what is shown in Fig. 5. As we can see, there is pattern appearing in the plot, and this has been explained in Appendix A. Darker regions imply a larger amount of nonunitarity present (in a percentage) for those values of E and L as depicted by the color bar on the right. Primarily, the wiggles arise due to the large δm^2 oscillations in the 1–4 sector. For long baseline neutrino experiments, $\sin^2(\lambda L/2) \simeq \mathcal{O}(1)$, which gives

$$\frac{\lambda L}{2} \simeq 1.57\left[\frac{\delta m^2_{31}}{2.5\times10^{-3}\,\mathrm{eV}^2}\frac{2.5\,\mathrm{GeV}}{E}\frac{L}{1300\,\mathrm{km}}\right] \quad \text{for DUNE} \tag{24}$$

for the first oscillation maximum (minimum) in the appearance (disappearance) channel. We note that $E = 1.5$ GeV and $L = 810$ km for NOvA and $E = 0.6$ GeV and $L = 295$ km for T2K (and also T2HK) also lead to $\lambda L \sim \pi$. The location of the first oscillation maximum (using $P_{\mu e}$) is also shown on the plot. Obviously, most of the ongoing or planned long baseline experiments lie on or close to[5] this curve.

The different colors depict the amount of unitarity violation. We can note that for the $\nu_e \to \nu_\alpha$ and the $\nu_\tau \to \nu_\alpha$ channel (where $\alpha = e,\ \mu,\ \tau$) the violation of unitarity is larger compared to the $\nu_\mu \to \nu_\alpha$ channel. This feature can be ascribed to the larger values of θ_{14} and θ_{34}

[5]NOvA is an off-axis experiment.

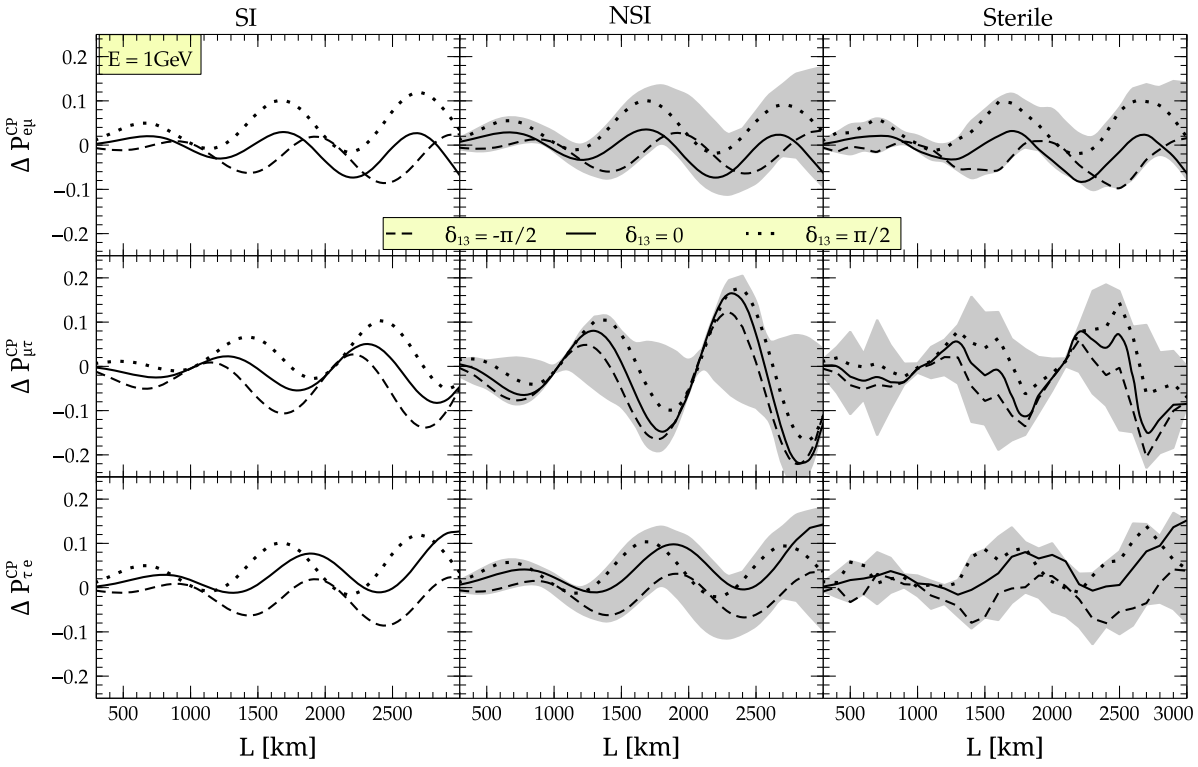

FIG. 2. *CP*-odd probability difference ($\Delta P^{CP}_{\alpha\beta}$) plotted as a function of the baseline at a fixed energy of $E = 1$ GeV. The three rows correspond to the different channels considered, while the three columns refer to effects due to SI, NSI, and sterile neutrino. The solid line corresponds to the case in which all *CP*-violating phases are set to zero including δ_{13}. The dotted (dashed) line corresponds to the case in which $\delta_{13} = \pi/2(\delta_{13} = -\pi/2)$ and all additional phases are set to zero. The gray bands in the cases of NSI and sterile neutrinos refer to the variation in phases of the additional parameters introduced in their allowed ranges along with the SI phase δ_{13} (see Tables I, II, and III for the values of the parameters used).

used in comparison to θ_{24} (see Table III). There is also a mild dependence on the value of δ_{13} as can be seen from different columns. Also, if we look at middle row ($\nu_\mu \to \nu_\alpha$ channel), it seems that none of the ongoing long baseline experiments can detect the presence of nonunitarity better than ∼6% or so.

C. Distinguishing intrinsic and extrinsic *CP* effects

In the context of long baseline experiments where matter can induce extrinsic *CP* effects, a nonzero value of $\Delta P^{CP}_{\alpha\beta}$ does not unequivocally imply intrinsic *CP* violation arising due to the Dirac *CP* phase (δ_{13}). To get over the problem of finding the source of *CP* violation (i.e., whether due to the intrinsic *CP* phase or due to the matter effects), other observables have been introduced [15] and can prove useful to establish whether *CP*-violation effects arise purely due to the Dirac-type *CP* phase (δ_{13}) or a combination of the intrinsic and extrinsic *CP* effects. We can define an observable quantity, which is obtained by taking the difference of the *CP* probability differences computed at different values of δ_{13} for the appearance as well as disappearance channels as follows [10,13,15]:

$$\begin{aligned}\delta[\Delta P^{CP}_{\alpha\beta}] &= [\Delta P^{CP}_{\alpha\beta}](\delta_{13} = \pi/2) - [\Delta P^{CP}_{\alpha\beta}](\delta_{13} = 0),\\ &= [P_{\alpha\beta} - \bar{P}_{\alpha\beta}](\delta_{13} = \pi/2)\\ &\quad - [P_{\alpha\beta} - \bar{P}_{\alpha\beta}](\delta_{13} = 0). \qquad (25)\end{aligned}$$

The choices of δ_{13} in the above equation allow for better observability of the intrinsic *CP* effects. Obviously, in vacuum, the second term on the rhs vanishes, and the first term gives completely intrinsic *CP* contribution, which will be nonzero for $\delta_{13} = \pi/2$. If matter effects are switched off, Eq. (25) reduces to the expression for vacuum asymmetry corresponding to *CP* violation [see Eqs. (17) and (18)]. In standard matter, both the first and second terms on the rhs will be nonzero in general. The second term being nonzero in matter signals the presence of purely extrinsic effects. Under certain conditions,[6] the matter contributions are independent of δ_{13} [i.e., not

[6]As we shall see, both vacuum and matter effects lead to the same difference in probability differences due to an interesting conspiracy near the first peak [62]. Note that this cancellation is perfect in the case of standard matter effects but starts getting imperfect in the case of new physics scenarios. This is due to the fact that δ_{13} and new physics terms appear in a coupled way in the probability expressions.

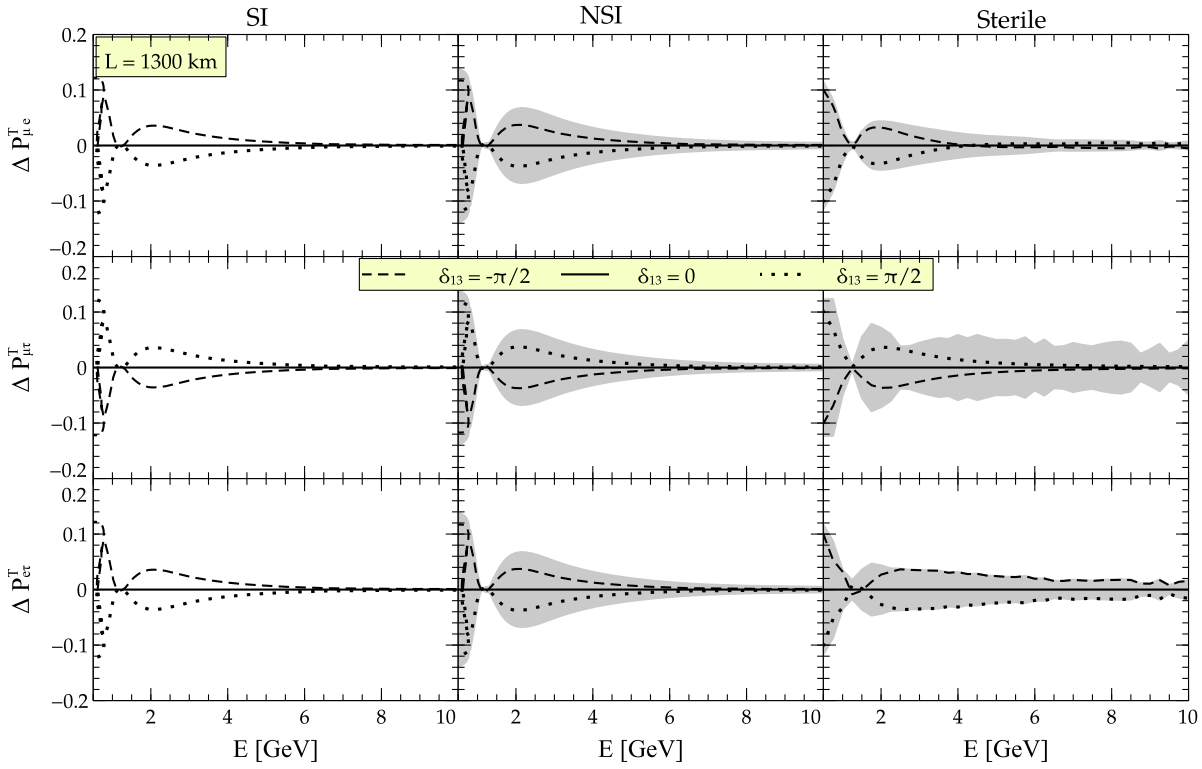

FIG. 3. Same as Fig. 1 but for T asymmetry.

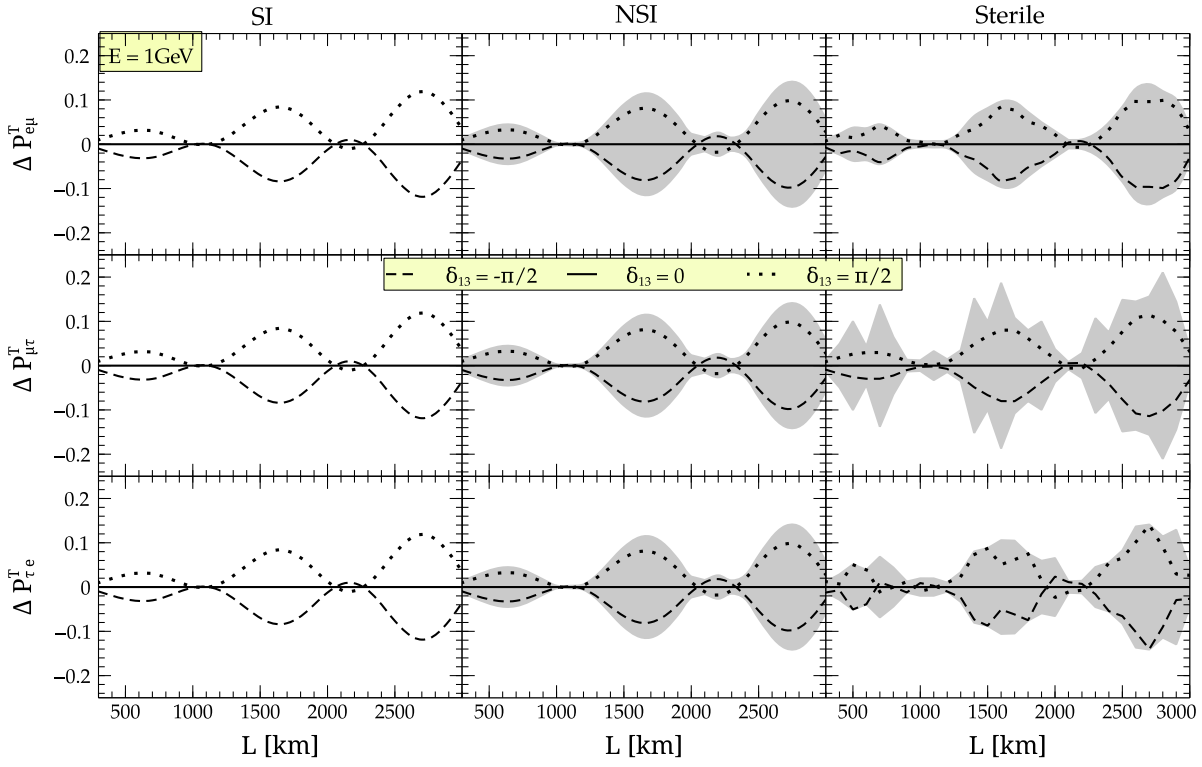

FIG. 4. Same as Fig. 2 but for T asymmetry.

TABLE II. The current bounds on NSI parameters taken from Ref. [54] (see also Refs. [55,56]). The phases $\varphi_{\alpha\beta}$ of the off-diagonal parameters are unconstrained and can lie the allowed range, $\varphi_{\alpha\beta} \in [-\pi, \pi]$.

ε_{ee}	$\lvert\varepsilon_{e\mu}\rvert$	$\lvert\varepsilon_{e\tau}\rvert$	$\lvert\varepsilon_{\mu e}\rvert$	$\varepsilon_{\mu\mu}$	$\lvert\varepsilon_{\mu\tau}\rvert$	$\lvert\varepsilon_{\tau e}\rvert$	$\lvert\varepsilon_{\tau\mu}\rvert$	$\varepsilon_{\tau\tau}$
<4.2	<0.3	<3.0	<0.3	$*$	<0.04	<3.0	<0.04	<0.15

TABLE III. The current bounds on sterile parameters taken from Refs. [57–61].

θ_{14} (°)	θ_{24} (°)	θ_{34} (°)	δ_{13} (°)	δ_{24} (°)	δ_{34} (°)	δm^2_{41} (eV^2)
8.0	5.0	15.0	$[-\pi, \pi]$	$[-\pi, \pi]$	$[-\pi, \pi]$	1.0

arising due to the intrinsic *CP* phase, δ_{13}; see Eq. (26) below], and the above quantity is helpful to extract the intrinsic contribution [62].

From Ref. [62], one can analytically see that for $\nu_\mu \to \nu_e$ oscillation

$$\Delta P^{CP}_{\mu e} = \Delta P^{CP}_{\mu e}(\sin\delta_{13}) + \Delta P^{CP}_{\mu e}(\text{matter}, \delta_{13}\text{-indep}) + \cdots, \tag{26}$$

which implies decoupling of the intrinsic and extrinsic effects may be possible near the peak energy. Of course, the decoupling is not expected to work in general.

In Figs. 6–8, we show the oscillograms of $\delta[\Delta P^{CP/T}_{\alpha\beta}]$ in the plane of E and L for the appearance and the disappearance channels. The three rows correspond to the different appearance or disappearance channels (as mentioned in the subscripts of quantities plotted on the y axes of the plots), while the columns are for the SI, NSI, and sterile neutrino cases. Unless otherwise stated, in this and the remaining plots, we take the additional phases in NSI and sterile neutrino cases to be zero for the sake of simplicity. These plots depict how new physics effects impact the inferences about intrinsic *CP* effects in the region in the E–L plane. Figure 8 is similar to Fig. 6 but shows the T asymmetry.

The following observations can be made in connection with the difference in *CP* asymmetries for the three appearance channels (see Fig. 6):

(i) $\nu_\mu \to \nu_e$ *channel.*—In the SI case, we note that the regions of large asymmetry ($\gtrsim$18%) are more concentrated at lower energies ($\lesssim$2 GeV). Any experiment operating at higher energies and longer baselines cannot probe intrinsic *CP* violation via the quantity considered. The whitish region around a

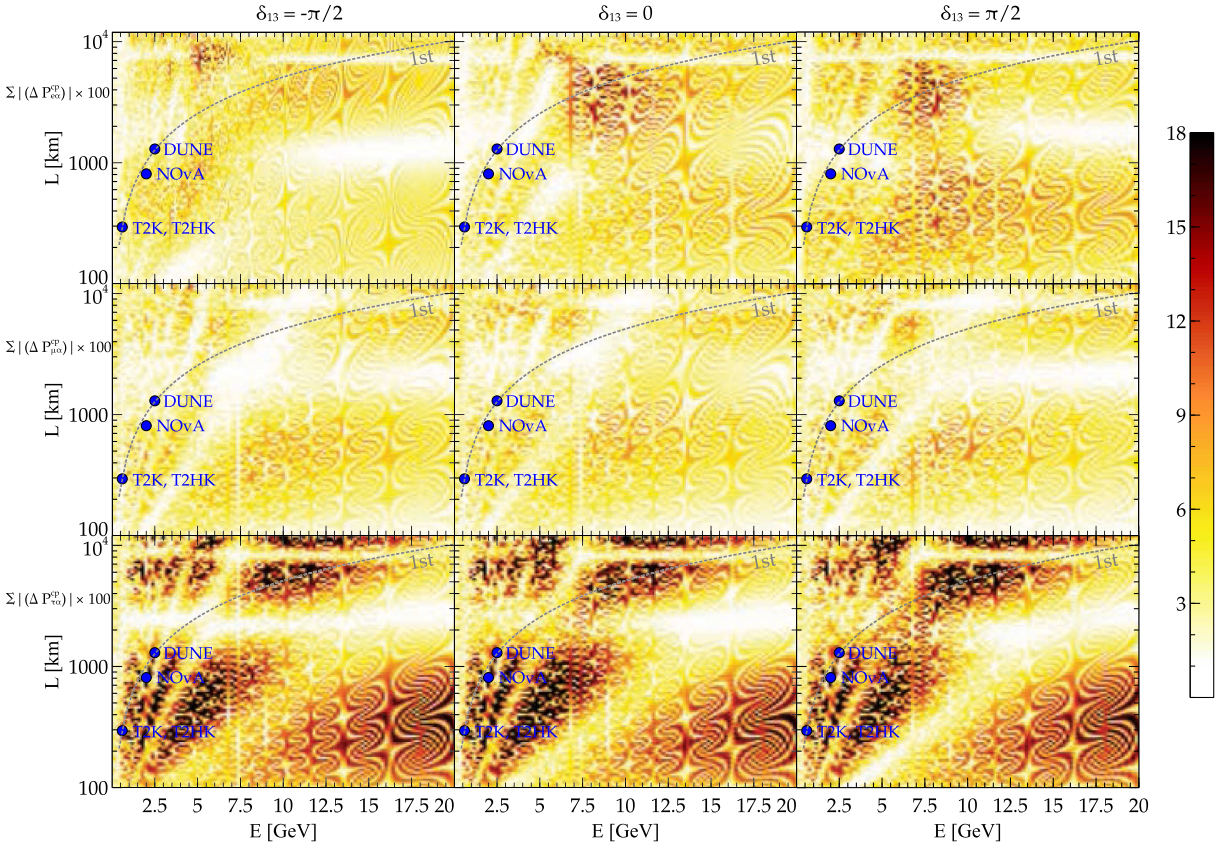

FIG. 5. Measure of nonunitarity ($\sum_\alpha |\Delta P^{CP}_{e\alpha}|$, $\sum_\alpha |\Delta P^{CP}_{\mu\alpha}|$, $\sum_\alpha |\Delta P^{CP}_{\tau\alpha}|$) in the sterile neutrino case shown in the plane of $E - L$. The additional phases δ_{24} and δ_{34} are set to zero. The location of the first oscillation maximum (for $P_{\mu e}$) is depicted by the dashed gray curve. Darker regions imply a larger amount of nonunitarity present (in a percentage) for those values of E and L.

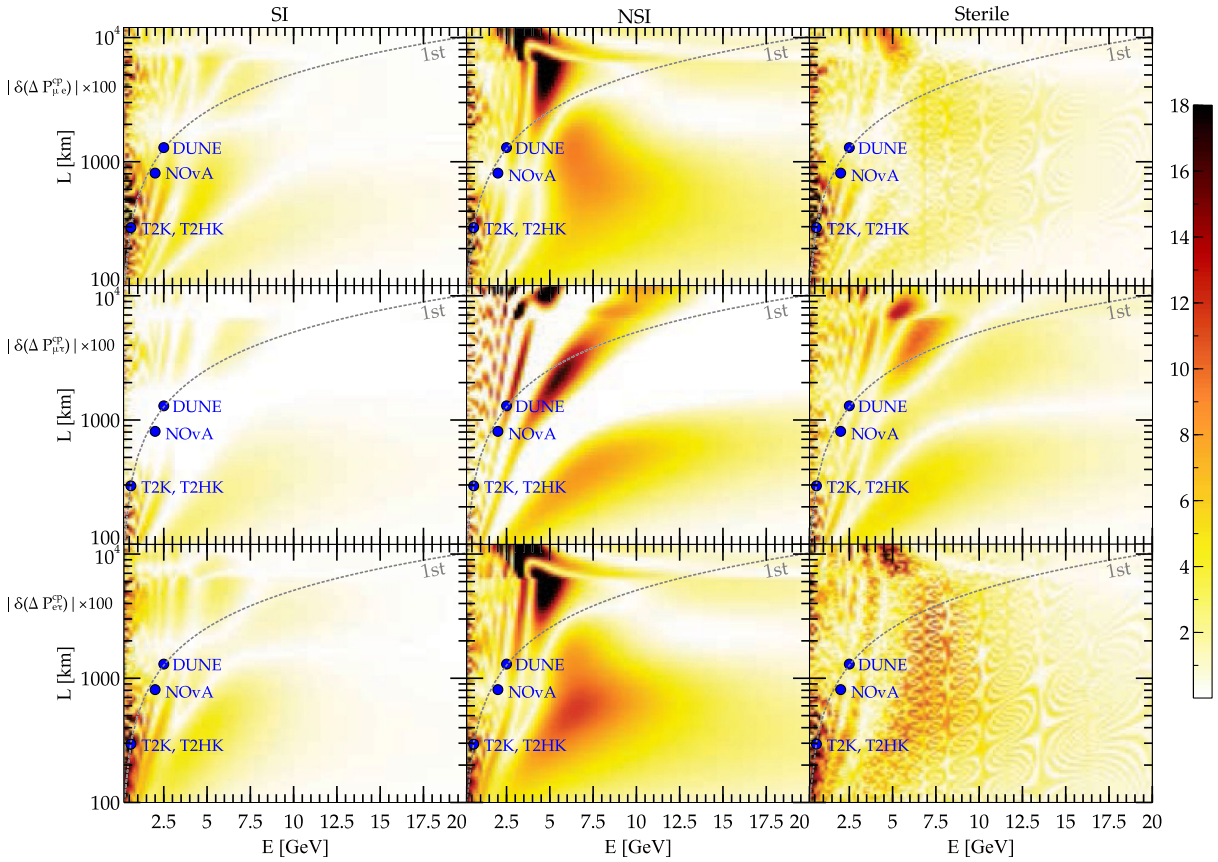

FIG. 6. Oscillogram of absolute relative *CP* asymmetry for the appearance channels. The location of first oscillation maximum (for $P_{\mu e}$) is depicted by dashed gray curve. Darker regions imply a larger amount absolute relative *CP* asymmetry (in a percentage) for those values of E and L.

baseline of ∼8000 km is due to the fact that it is near the magic baseline where the *CP* dependence vanishes [63]. For the NSI and sterile neutrino cases, we see the pattern in the oscillogram changes. However in case of NSI, the changes are more drastic. The new significant dark patches in the NSI case can be accounted for by assuming a nonzero value of a particular NSI parameter (see Appendix B). The origin of different colors can be attributed to different parameters. For instance, in the $\nu_e \to \nu_\mu$ and $\nu_e \to \nu_\tau$ channels, the orangeish patch (∼8%–10%) that lies in $E \in (5\text{–}9)$ GeV, $L \in (300\text{–}2000)$ km is due to the presence of ε_{ee}. The sterile neutrino case is similar to SI with new features in the entire oscillogram plot. The wiggles arise due to the fast oscillations induced by δm^2_{41}, which is large in comparison to the other mass squared splittings. Among the considered experiments, T2K and T2HK seem to have the potential to extract the intrinsic *CP* phase from the probability-level discussion as far as the $\nu_\mu \to \nu_e$ channel is concerned.

(ii) $\nu_\mu \to \nu_\tau$ *channel*.—Using this channel, extracting intrinsic *CP* violation is hard as can be seen from large whitish regions in the oscillogram for the SI case. Again, the pattern is very different for the NSI and sterile neutrino cases. From the probability-level oscillogram in the $\nu_\mu \to \nu_\tau$ channel, we note that in the NSI case DUNE lies on a darker patch. This gives an impression that in the presence of NSI extraction of the intrinsic *CP* phase may be easier than in the SI case. However, this is misleading since the source of intrinsic *CP* violation remains the same in both cases (NSI phases are set to zero). The substructures cancel in the sterile neutrino case due to the fact that the wiggles are independent of δ_{13} (see Fig. 13 in Appendix C).

(iii) $\nu_e \to \nu_\tau$ *channel*.—The gross features are similar to the $\nu_\mu \to \nu_e$ channel. The darker regions can be understood from the size of the wiggles in Fig. 13 in Appendix C.

The following observations can be made in connection with *CP* plots for the three disappearance channels (see Fig. 7):

(i) $\nu_e \to \nu_e$ *channel*.—There is no δ_{13} dependence in the $\nu_e \to \nu_e$ channel [64], and hence the SI oscillogram is blank. NSI introduces significant effect in this channel. The features can be understood from Appendix B. Also, in the sterile neutrino case, there are smaller dark patches as well as wiggles.

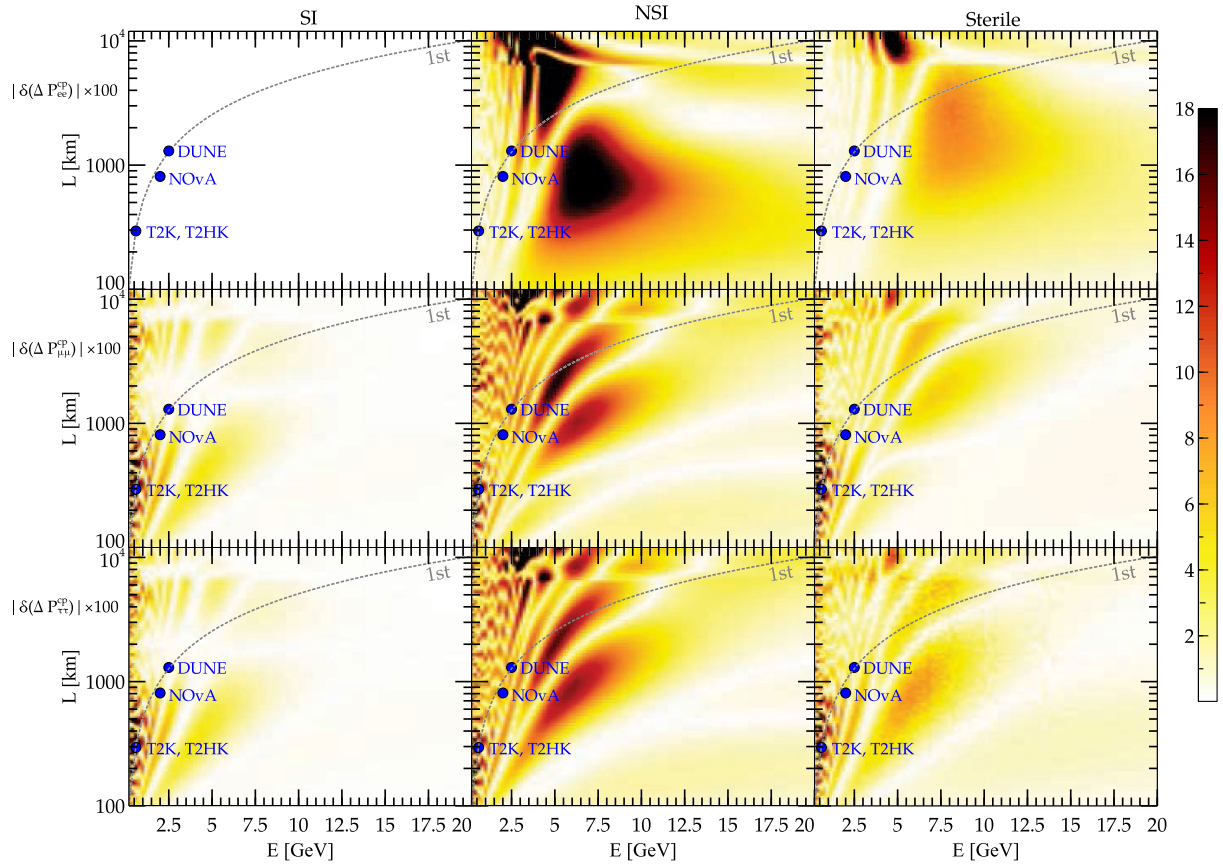

FIG. 7. Oscillogram of absolute relative *CP* asymmetry for the disappearance channels. The location of the first oscillation maximum (for $P_{\mu e}$) is depicted by the dashed gray curve. Darker regions imply a larger amount of absolute relative *CP* asymmetry (in a percentage) for those values of E and L.

(ii) $\nu_\mu \to \nu_\mu$ *channel*.—Here, the dependence on δ_{13} is mild for the SI case [64]. Again, differences arise in case of NSI and sterile neutrino.

(iii) $\nu_\tau \to \nu_\tau$ *channel*.—Here, the dependence on δ_{13} is mild and similar to the case of the $\nu_\mu \to \nu_\mu$ channel for the SI case [64]. For NSI and sterile neutrino cases, we see darker regions and wiggles, respectively.

The following observations can be made in connection with T asymmetry plots for the three appearance channels (Fig. 8). The oscillograms show features similar in nature to the *CP* case, but there are fewer dark patches than in the *CP* case. Though the SI and NSI cases are indistinguishable, wiggles appear in the sterile neutrino case.

IV. IMPLICATIONS FOR LONG BASELINE ACCELERATOR EXPERIMENTS

Below, we give a very brief description of the long baseline experiments considered to describe the implications of our results at the level of event rates [for more details, please see Table IV (see also Ref. [20])]:

(i) *DUNE*.—We consider a design that uses a 120 GeV proton beam with a power of 1.0 MW, which corresponds to

$$\frac{\text{Protons on target (P.O.T.)/year}}{[5.0\times 10^{20}]} \sim \frac{\text{Proton beam power}}{[1\ \text{MW}]} \times \frac{T}{[10^7\ \text{sec}]} \times \frac{[120\ \text{GeV}]}{E_p}. \tag{27}$$

We assume five years of run time in both the neutrino and antineutrino modes. The total exposure is around 350 kt MW yr.

(ii) *NOvA experiment*.—We consider a design that uses a 120 GeV proton beam with a power of 0.7 MW, which corresponds to

$$\frac{\text{P.O.T/year}}{[3.0\times 10^{20}]} \sim \frac{\text{Proton beam power}}{[0.7\ \text{MW}]} \times \frac{T}{[10^7\ \text{sec}]} \times \frac{[120\ \text{GeV}]}{E_p}. \tag{28}$$

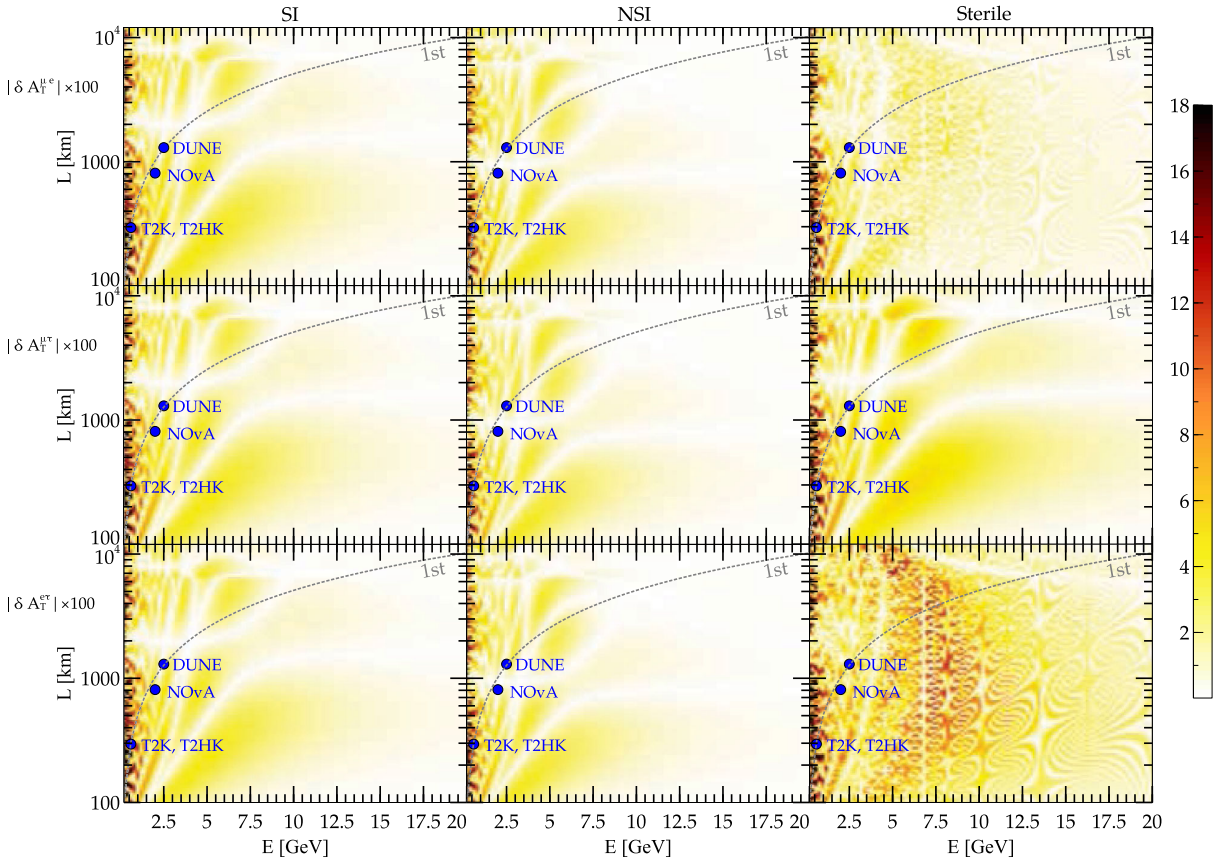

FIG. 8. Oscillogram of absolute relative T asymmetry for the appearance channels. The location of the first oscillation maximum (for $P_{\mu e}$) is depicted by the dashed gray curve. Darker regions imply larger amount absolute relative T asymmetry (in a percentage) for those values of E and L.

We assume three years of run time in both the neutrino and antineutrino modes. The total exposure is around 84 kt MW yr.

(iii) *T2K*.—We consider a design that uses a 50 GeV proton beam with a power of 0.770 MW, which corresponds to

$$\frac{\text{P.O.T./year}}{[4.15\times10^{20}]}\sim\frac{\text{Proton beam power}}{[0.770\text{ MW}]}\times\frac{T}{[10^7\text{ sec}]}\times\frac{[50\text{ GeV}]}{E_p}. \quad (29)$$

We assume three years of run time in both the neutrino and antineutrino modes. The total exposure is around 103.95 kt MW yr

(iv) *T2HK*.—We consider a design that uses a 30 GeV proton beam with a power of 7.5 MW, which corresponds to

$$\frac{\text{P.O.T./year}}{[8.0\times10^{21}]}\sim\frac{\text{Proton beam power}}{[7.5\text{ MW}]}\times\frac{T}{[10^7\text{ sec}]}\times\frac{[30\text{ GeV}]}{E_p}. \quad (30)$$

We assume three years and one year of run time in the neutrino and antineutrino modes, respectively. The total exposure is around 16.8 Mt MW yr.

We present our results at the level of event rates using the following quantity:

$$\delta[\Delta N^{CP}_{\alpha\beta}]=[\Delta N^{CP}_{\alpha\beta}](\delta_{13}=\pi/2)-[\Delta N^{CP}_{\alpha\beta}](\delta_{13}=0). \quad (31)$$

Here, the first term on the rhs corresponds to the case of maximal CP violation ($\delta_{13}=\pi/2$), while the second term corresponds to CP conservation ($\delta_{13}=0$). Since all the accelerator experiments mentioned above can produce ν_μ only at the source (pion decay), we discuss the implications of our results at the level of event rates using $\nu_\mu\to$ any flavor. Note that the binning and energy range of the experiments are different (see Table IV):

(i) $\nu_\mu\to\nu_e$.—Among all the considered experiments, the total event rate is highest for T2HK by a large margin. This high statistics is due to the large detector size and beam power. Moreover, this means that one would be able to disentangle intrinsic and extrinsic sources of CP violation better with T2HK. The much shorter baseline ensures that matter effects

TABLE IV. Detector configuration, efficiencies, resolutions, and relevant energy ranges for DUNE, NOvA, T2K, and T2HK.

DUNE:	T2K:
$E_p = 2.5$ GeV, $L = 1300$ km Run time (yr) $= 5\nu + 5\bar{\nu}$ 35 kton, Liquid argon time projection chamber $\varepsilon_{\rm app} = 80\%$, $\varepsilon_{\rm dis} = 85\%$ $R_\mu = 0.20/\sqrt{E}$, $R_e = 0.15/\sqrt{E}$ $E \in [0.5 - 10.0]$ GeV, bin width $= 250$ MeV	$E_p = 0.6$ GeV, $L = 295$ km Run time (yr) $= 3\nu + 3\bar{\nu}$ 22.5 kton, Water Cerenkov $\varepsilon_{\rm app} = 50\%$, $\varepsilon_{\rm dis} = 90\%$ $R_\mu = 0.085/\sqrt{E}$, $R_e = 0.085/\sqrt{E}$ $E \in [0.4 - 1.2]$ GeV, bin width $= 40$ MeV
NOvA: $E_p = 1.6$ GeV, $L = 810$ km Run time (yr) $= 3\nu + 3\bar{\nu}$ 14 kton, Totally active Scintillator detector $\varepsilon_{\rm app} = 55\%$, $\varepsilon_{\rm dis} = 85\%$ $R_\mu = 0.06/\sqrt{E}$, $R_e = 0.085/\sqrt{E}$ $E \in [0.5 - 4.0]$ GeV, bin width $= 125$ MeV	T2HK: $E_p = 0.6$ GeV, $L = 295$ km Run time (yr) $= 1\nu + 3\bar{\nu}$ 560 kton, Water Cerenkov $\varepsilon_{\rm app} = 50\%$, $\varepsilon_{\rm dis} = 90\%$ $R_\mu = 0.085/\sqrt{E}$, $R_e = 0.085/\sqrt{E}$ $E \in [0.4 - 1.2]$ GeV, bin width $= 40$ MeV

TABLE V. $|\delta[\Delta N^{CP}_{\alpha\beta}]| = |[\Delta N^{CP}_{\alpha\beta}](\delta_{13} = \pm\pi/2) - [\Delta N^{CP}_{\alpha\beta}](\delta_{13} = 0)|$ summed over energy bins for different experiments for NH and IH. For NSI, we show the collective case when the NSI parameters $|\varepsilon_{e\mu}| = 0.04, |\varepsilon_{e\tau}| = 0.04, |\varepsilon_{\mu\tau}| = 0.03, \varepsilon_{\mu\mu} = 0.06, \varepsilon_{\tau\tau} = 0.1, \varepsilon_{ee} = 0.4$, $\varphi_{e\mu} = 0$, $\varphi_{e\tau} = 0$, and $\varphi_{\mu\tau} = 0$ are considered. The sterile parameters are as mentioned in Table III.

	SI		NSI		Sterile	
Experiment	$\nu_\mu \to \nu_e$	$\nu_\mu \to \nu_\mu$	$\nu_\mu \to \nu_e$	$\nu_\mu \to \nu_\mu$	$\nu_\mu \to \nu_e$	$\nu_\mu \to \nu_\mu$
DUNE (NH, $\pi/2$)	345	91	644	252	325	60
DUNE (NH, $-\pi/2$)	328	91	261	252	197	60
DUNE (IH, $\pi/2$)	231	41	141	187	227	28
DUNE (IH, $-\pi/2$)	310	41	514	187	278	28
NOvA (NH, $\pi/2$)	40	19	59	41	43	12
NOvA (NH, $-\pi/2$)	34	19	16	41	22	12
NOvA (IH, $\pi/2$)	33	12	15	36	38	9
NOvA (IH, $-\pi/2$)	36	12	53	36	43	9
T2K (NH, $\pi/2$)	22	4	26	6	23	3
T2K (NH, $-\pi/2$)	15	4	11	6	8	3
T2K (IH, $\pi/2$)	14	3	11	5	22	3
T2K (IH, $-\pi/2$)	21	3	24	5	21	3
T2HK (NH, $\pi/2$)	2142	44	2575	273	1954	55
T2HK (NH, $-\pi/2$)	2001	44	1567	273	1492	55
T2HK (IH, $\pi/2$)	2021	32	1574	217	2552	71
T2HK (IH, $-\pi/2$)	2094	32	2531	217	2658	71

are small, which in turn simplifies the extraction of the intrinsic *CP* phase. We can note that the NSI and sterile neutrino scenarios also retain this feature as long as additional phases are set to zero (see Table V and Fig. 9).

(ii) $\nu_\mu \to \nu_\mu$.—Here, in the case of SI, DUNE seems to be the best choice. But in the presence of new physics such as NSI or sterile neutrinos, T2HK seems to do slightly better, though DUNE is also competitive (see Table V and Fig. 10).

(iii) $\nu_\mu \to \nu_\tau$.—The number of events is scarce even after using a higher-energy beam tune, and evidently we cannot draw useful conclusions from this channel (see Table V and Fig. 11).

V. CONCLUDING REMARKS

It is fair to say that neutrino oscillation physics has entered a precision era, and the upcoming long baseline experiments are expected to shed some light on one of the crucial unknown parameters in the oscillation framework: the leptonic *CP* phase. Going beyond the recent studies revealing how potential new physics scenarios can hinder the clean determination of this important parameter

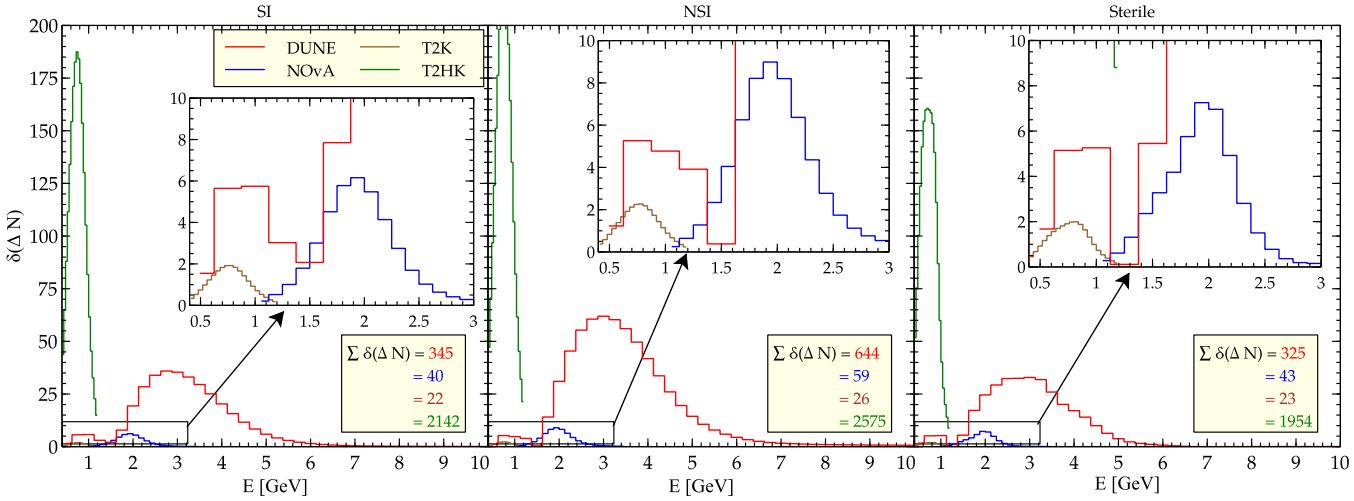

FIG. 9. $|\delta[\Delta N_{\mu e}^{CP}]|$ plotted as a function of E. The binning for the four experiments is different.

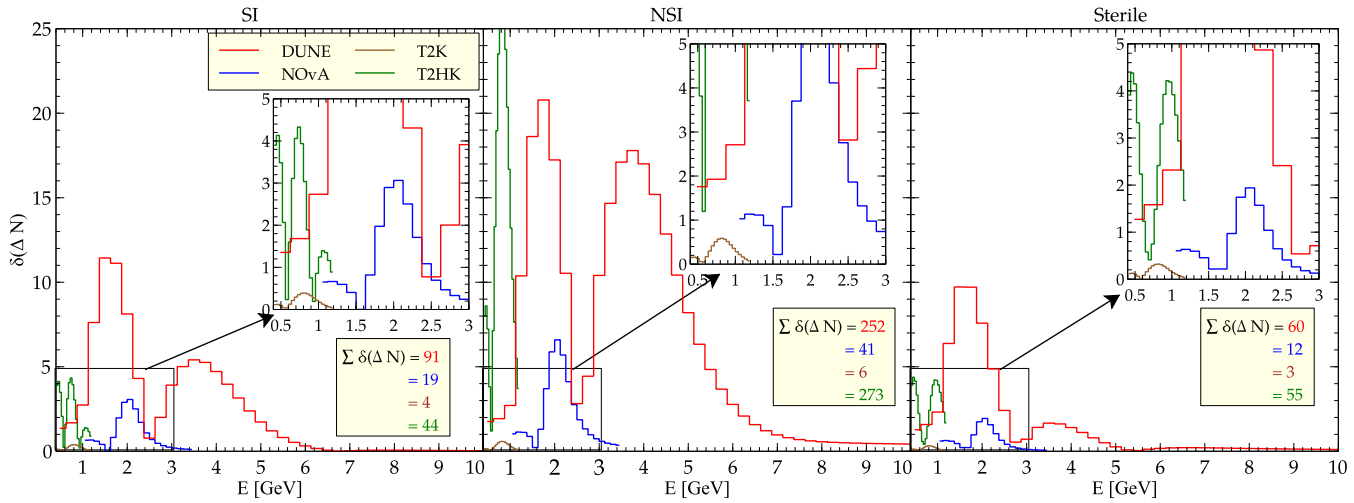

FIG. 10. $|\delta[\Delta N_{\mu\mu}^{CP}]|$ plotted as a function of E. The binning for the four experiments is different.

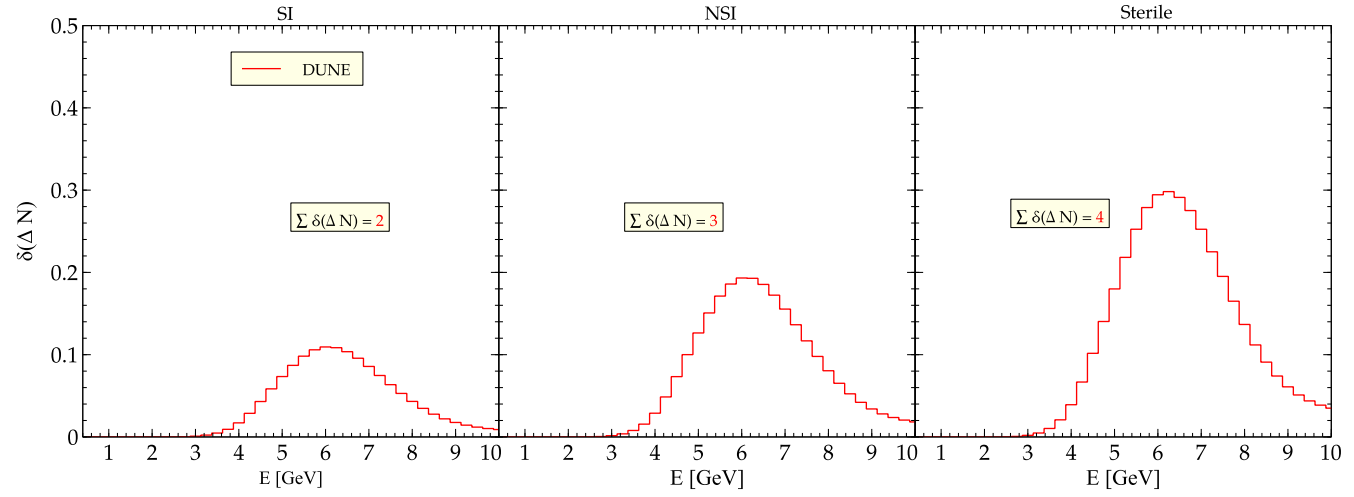

FIG. 11. $|\delta[\Delta N_{\mu\tau}^{CP}]|$ plotted as a function of E. We get a handful events for DUNE and none for the rest.

[17–34], we have addressed the issue of clean separation of the intrinsic leptonic CP phase from the extrinsic contribution arising due to SI as well as new physics.[7] We have also shown the impact of new physics on testing nonunitarity.

Accelerator-based long baseline experiments are plagued with the problem of clean separation of intrinsic and extrinsic CP-violating terms due to the fact that neutrinos propagate through Earth matter. Resolution of this is a difficult task, and there are several suggestions including new observables in the literature. To elucidate and quantify our results, we have used an observable quantity given by Eq. (25) (see Refs. [10,13,15]) and scanned the range of energies and path lengths relevant to long baseline experiments. We have considered two new physics scenarios: NSI in propagation and additional sterile neutrinos. We have depicted our outcome in the form of oscillogram plots in $L-E$ space where we unraveled the regions where the impact of new physics on the oscillograms could be potentially large. We have also highlighted the differences in the different physics cases for some benchmark values of new physics parameters. Our discussion has been mostly targeted toward accelerator-based neutrino experiments with $L/E \sim 500$ km/GeV but can easily be extended to short baseline experiments and very long baseline experiments. Other than the question of separating the intrinsic CP contribution, we have also discussed the impact of additional sterile neutrinos on the unitarity conditions.

For the sake of simplicity, we have set the additional intrinsic CP phases (induced by new physics) to zero and discussed the impact of additional parameters appearing in NSI and sterile neutrino cases that are extrinsic in nature. Further, through the event rates [see Eq. (31)] for realistic configurations for some of the ongoing and planned long baseline experiments, we have shown which experiment has the better potential to answer the questions that we have posed in this article. We have considered four long baseline experiments, T2K, T2HK, DUNE, and NoVA, and also taken into account both the appearance ($\nu_\mu \to \nu_e$) and disappearance ($\nu_\mu \to \nu_\mu$) channels for each of them (see Sec. IV). We have demonstrated how even the restricted class of CP-conserving new physics effects complicate the separation of the intrinsic CP phase from the extrinsic CP effects that can come from SI or new physics. Our main results can be summarized as follows:

(i) *Nonunitarity.*—Deviation from unitarity (in the sterile neutrinos case) at the probability level can be discernible by looking at various E and L ranges where one gets darker regions. Figure 5 shows the deviation from unitarity for three different values of δ_{13}. Obviously, in vacuum, one would expect to get a blank region whenever the source of the CP-violating phase vanishes [δ_{13} being the only source of CP violation; see Eq. (12)]. This corresponds to the middle column of Fig. 5. Instead, we see some pattern even for $\delta_{13}=0$, and this can be attributed to the SI with matter which contributes to nonunitarity. We can note that only in channels involving ν_τ might it be possible for DUNE or NOvA or T2HK to reveal some signature of nonunitarity. However, this is not expected to be useful at the level of events. Nonunitarity is very hard to probe in the ν_τ channel using any of the long baseline experiments primarily because one is statistically limited in case of tau events (see Fig. 5).

(ii) *Extraction of the intrinsic CP-violating component and comparison of new physics scenarios with SI.*—At the probability level, the darker shaded regions imply a larger influence of new physics. This dark region should not be thought of as aiding the extraction of the intrinsic CP component in any given channel; rather, it makes the situation more complicated. Some of the ongoing and future experiments are shown as bulleted points along the curve representing the first oscillation maximum. For lower values of E and L, it is expected that the NSI effects would be small, and hence one could in principle have a clean detection of the intrinsic component. From the oscillograms, we can note that the impact of new physics scenarios is more prominent at larger values of E and L. Also, note that NoVA and DUNE lie in the lighter shaded region of the oscillogram, while T2K (and T2HK) is in a darker patch. Hence, the baseline choice of T2K or T2HK is desirable in order to extract the intrinsic component from the probability-level analysis. Finally, at the level of events, T2HK wins due to the large statistics in order to cleanly extract the intrinsic contribution (see Figs. 6–8).

(iii) *Event analysis.*—At the level of event rates, we have found that T2HK offers the best statistics among all the considered experiments in the case of the $\nu_\mu \to \nu_e$ channel. But DUNE is competitive with T2HK if we consider $\nu_\mu \to \nu_\mu$ channel. The tau appearance channel is mostly not useful due to limited statistics (see Figs. 9–11 and Table V).

Finally, some comments concerning the validity of our approach are in order. We assume that the only source of intrinsic CP violation is due to δ_{13}, which is very optimistic. In principle, the new physics scenarios considered here can also bring in more sources of intrinsic CP violation via pure phase terms. Any source of new physics therefore has both intrinsic (i.e., phases) and extrinsic components, and discussing the problem with both components is rather cumbersome. In fact, the separation of

[7]We assume that the only source of intrinsic CP violation is due to δ_{13}, which is very optimistic. In principle, the new physics scenarios considered here can also bring in more sources of intrinsic CP violation via pure phase terms.

intrinsic contribution using a quantity like $\delta(\Delta P^{CP}_{\alpha\beta})$ is feasible only when there is one source of intrinsic CP violation (δ_{13}) present. For a more general scenario with phases introduced in the new physics sector, one needs to think of appropriate observables to be able to separate out the intrinsic contribution.

Nonetheless, we would like to stress that our overall approach to survey the impact of CP-conserving new physics scenarios is quite general and can be applied to other new physics scenarios or other regimes in $E-L$ space. The discussion in the present work has been targeted toward accelerator-based neutrino experiments with $L/E \sim 500\,\mathrm{km/GeV}$, but the ideas can easily be extended to short baseline experiments or very long baseline experiments.

ACKNOWLEDGMENTS

It is a pleasure to thank Raj Gandhi for useful discussions and critical comments on the manuscript. We acknowledge the use of the HRI cluster facility to carry out computations in this work. J. R. acknowledges financial support in the form of a research fellowship from UGC-BSR [Ref. No. F.25-1/2013-14(BSR)/7-95/2007(BSR)]. M. M. would like to thank Jawaharlal Nehru University (JNU) and Utpal Chattopadhyay at Indian Association for Cultivation of Science, Kolkata, for academic visits and support from the DAE neutrino project at Harish-Chandra Research Institute (HRI) during the progress of the present work. The work of M. M. was funded by the Spanish Grants No. FPA2014-58183-P, No. SEV-2014-0398 (MINECO), and No. PROMETEOII/2014/084 (Generalitat Valenciana). M. M. and P. M. would like to thank HRI for a visit during the finishing stages of this work. P. M. acknowledges support from University Grants Commission under the second phase of University with Potential of Excellence at JNU and DST-PURSE grant at JNU as well as partial support from the European Unions Horizon 2020 Research and Innovation Programme under Marie Sklodowska-Curie Grant No. 674896. We would like to thank the anonymous referees for constructive suggestions.

APPENDIX A: ORIGIN OF OSCILLOGRAM PATTERN DEPICTING NONUNITARITY IN THE STERILE NEUTRINO CASE

To explain the features of different panels in Fig. 5, in Fig. 12, we show the individual components (blue, black, and dark green curves) and the sum of the contributions in each row (red curves) appearing in Fig. 5 for a fixed baseline of 1300 km. As we can see, the red curve is rapidly

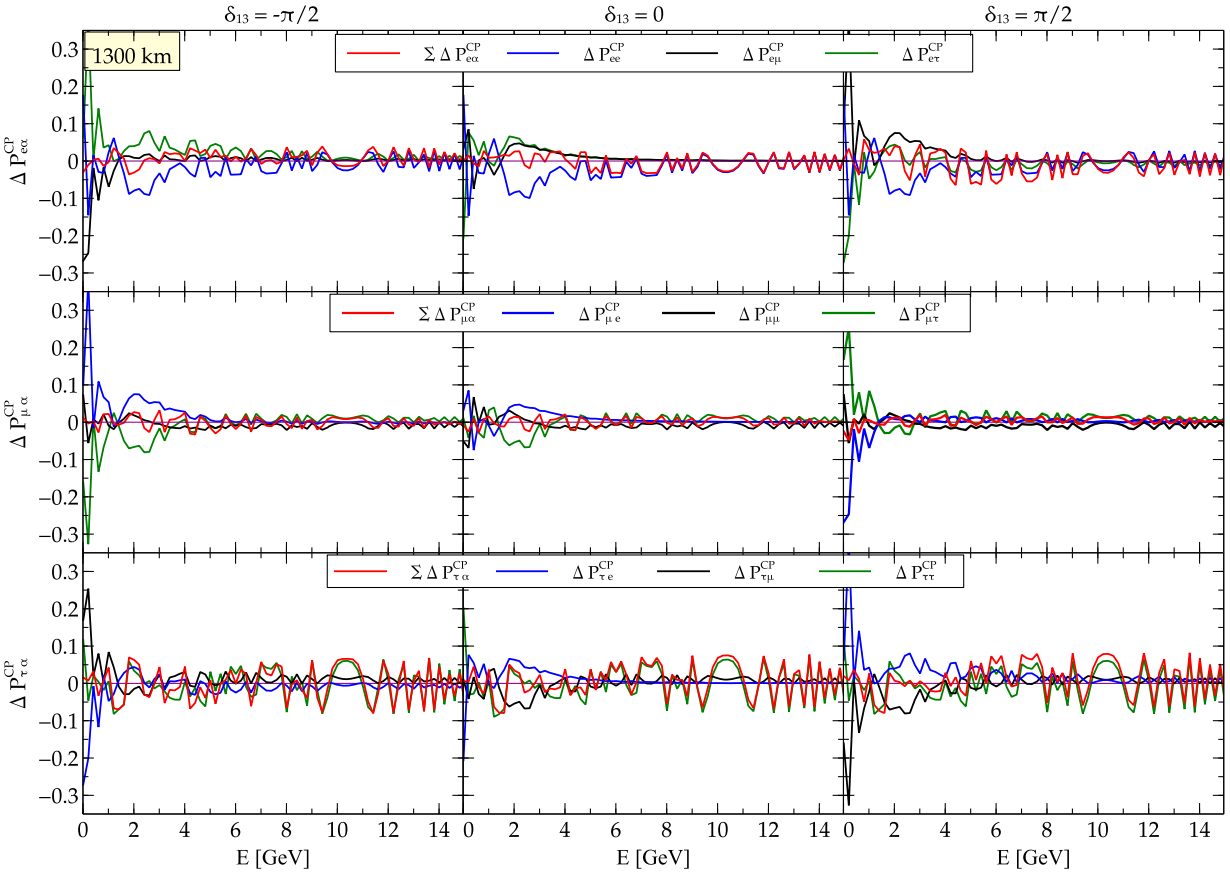

FIG. 12. $\Delta P^{CP}_{e\alpha}$, $\Delta P^{CP}_{\mu\alpha}$, and $\Delta P^{CP}_{\tau\alpha}$ plotted as a function of E for a fixed baseline of 1300 km.

oscillating, which leads to thin light and dark patches in Fig. 5 along the horizontal line at 1300 km. The amplitude of the red curve depends on the value of the sterile mixing angle relevant in each channel (see the main text).

APPENDIX B: ORIGIN OF DARK REGIONS IN THE *CP* AND *T* OSCILLOGRAMS IN THE NSI CASE

The approximate analytic expressions for probabilities up to second order in small parameters ($\hat{r_A}, s_{13}, \varepsilon$'s) in different channels in the case of NSI are given in Refs. [65–67]. Using the analytic expressions, we attempt to explain the distinct features of the oscillograms (Figs. 6, 7, and 8). To simplify the tedious expressions, we assume the following:

(i) There is normal hierarchy.
(ii) $|\varepsilon_{e\mu}| = |\varepsilon_{e\tau}|$, which is consistent with our choice of parameters in generating the oscillograms. this results in the cancellation of terms $\propto (|\varepsilon_{e\mu}| - |\varepsilon_{e\tau}|)$ and allows for useful simplifications in the analytical formulas.
(iii) The NSI phases are set to zero ($\varphi_{e\mu} = \varphi_{e\tau} = \varphi_{\mu\tau} = 0$).
(iv) Up to second order, the expression for $P(\nu_e \to \nu_\alpha)$ (where, $\alpha = e, \mu, \tau$) contains the NSI parameters $\varepsilon_{e\mu}, \varepsilon_{e\tau}, \varepsilon_{ee}$ [65]. Hence, the mild effect of $\varepsilon_{\mu\tau}, \varepsilon_{\mu\mu}, \varepsilon_{\tau\tau}$ on the electron sector cannot be understood from these.
(v) To get the antineutrino probabilities, one needs to do the following replacements: $r_A \to -r_A$, $\delta_{13} \to -\delta_{13}$, $\varepsilon_{\alpha\beta} \to \varepsilon^*_{\alpha\beta}$.

In order to facilitate the presentation, we define the following quantities (the bars above indicate the corresponding quantities for antineutrinos):

(1)

$$r_A = \frac{A}{\Delta m^2_{31}} \approx 0.03\, E[\mathrm{GeV}]\rho[gm/cc],$$
$$\hat{r_A} = r_A(1 + \varepsilon_{ee}),$$
$$\lambda = \frac{\Delta m^2_{31}}{2E}. \tag{B1}$$

(2)

$$C = \frac{\hat{r_A}}{\sqrt{2}}(|\varepsilon_{e\mu}| + |\varepsilon_{e\tau}|); \quad \bar{C} = -C$$
$$D_1 = \frac{\sin((1-\hat{r_A})\lambda L/2)}{1-\hat{r_A}} - \frac{\sin((1+\hat{r_A})\lambda L/2)}{1+\hat{r_A}};$$
$$\bar{D_1} = -D_1$$
$$D_2 = \frac{\sin((1-\hat{r_A})\lambda L/2)}{1-\hat{r_A}} + \frac{\sin((1+\hat{r_A})\lambda L/2)}{1+\hat{r_A}};$$
$$\bar{D_2} = D_2$$
$$D = \frac{\sin((1-\hat{r_A})\lambda L/2)}{(1-\hat{r_A})^2} - \frac{\sin((1+\hat{r_A})\Delta)}{(1+\hat{r_A})^2};$$
$$\bar{D} = -D. \tag{B2}$$

(3)

$$\Omega = |\Omega| e^{i\omega} \quad \text{where}$$
$$|\Omega| \approx \sqrt{\frac{s^2_{13} + C^2 + 2 s_{13} C \cos\delta_{13}}{\hat{r_A}^2}},$$
$$\tan\omega = \frac{C\sin\delta_{13}}{s_{13} + C\cos\delta_{13}}, \quad \text{and}$$
$$|\bar{\Omega}| \approx \sqrt{\frac{s^2_{13} + C^2 - 2 s_{13} C \cos\delta_{13}}{\hat{r_A}^2}},$$
$$\tan\bar{\omega} = \frac{C\sin\delta_{13}}{s_{13} - C\cos\delta_{13}}. \tag{B3}$$

Note that ω vanishes at $\delta_{13} = 0$.

(4)

$$\Sigma = |\Sigma| \exp\{i\sigma\} \quad \text{where}$$
$$|\Sigma| = (r_\lambda/2r_A)\sin 2\theta_{12} + (\propto (|\varepsilon_{e\mu}| - |\varepsilon_{e\tau}|))$$
$$\approx (r_\lambda/2r_A)\sin 2\theta_{12},$$
$$\sigma \simeq \delta_{13} \quad \text{for } \varphi_{\alpha\beta} = 0. \tag{B4}$$

Hence, $|\bar{\Sigma}| = -|\Sigma|$ and $\bar{\sigma} = -\sigma$.

Now, we give the simplified expressions for the different sectors below.

1. $\mu - \tau$ sector

$$\delta\Delta P^{CP}_{\mu\tau} = \delta(P_{\mu\tau} - \bar{P}_{\mu\tau})$$
$$= (P_{\mu\tau} - \bar{P}_{\mu\tau})|_{\delta_{13}=\pi/2} - (P_{\mu\tau} - \bar{P}_{\mu\tau})|_{\delta_{13}=0}$$
$$\approx 4 s_{13} C \sin\lambda L/2 \left\{ \cos(\hat{r_A}\lambda L/2) D - \lambda L/2 (\cos\lambda L/2) \frac{2 r_A}{1 - \hat{r_A}^2} \right\} + r_\lambda \sin 2\theta_{12} \sin(\hat{r_A}\lambda L/2) \sin\lambda L/2 \sin\theta_{13} D_1. \tag{B5}$$

$$\begin{aligned}\delta\Delta P^{CP}_{\mu\mu} &= \delta(P_{\mu\mu} - \bar{P}_{\mu\mu}) \\ &= (P_{\mu\mu} - \bar{P}_{\mu\mu})|_{\delta_{13}=\pi/2} - (P_{\mu\mu} - \bar{P}_{\mu\mu})|_{\delta_{13}=0} \\ &\approx 4s_{13}C\left(D_1D_2 + \frac{\hat{r_A}\lambda L/2\sin(\lambda L)}{1-\hat{r_A}^2} - D\cos(\hat{r_A}\lambda L/2)\sin\lambda L/2\right) \\ &\quad + 2r_\lambda \sin 2\theta_{12}\cos\lambda L/2\frac{\sin(\hat{r_A}\lambda L/2)}{\hat{r_A}}\left[s_{13}D_2 + \frac{2C\sin((1+\hat{r_A})\lambda L/2)}{1+\hat{r_A}}\right]. \end{aligned} \tag{B6}$$

These expressions serve to explain the qualitative features obtained in Figs. 6 and 7. We note that $\delta\Delta P^{CP}_{\mu\tau}$ and $\delta\Delta P^{CP}_{\mu\mu}$ are shown in the middle row of Figs. 6 and 7, respectively. In Figs. 13 and 14, different terms in Eqs. (B5) and (B6) have been plotted, respectively, and we can connect these plots with Figs. 6 and 7. We observe the following distinct features from Figs. 13:

(i) The gross nature of $|\delta\Delta P^{CP}_{\mu\tau}|$ and $|\delta\Delta P^{CP}_{\mu\mu}|$ (the red curves) is mostly dictated by the first term ($\propto Cs_{13}$) in Eqs. (B5) and (B6), respectively. The first term is purely the NSI term and is the dominant term in the expression. Note that the second term in Eqs. (B5) and (B6) is scaled by r_λ ($\approx 10^{-2}$), which is small in comparison to the first term.

(ii) Let us compare the plots at different baselines. For shorter baselines, $|\delta\Delta P^{CP}_{\mu\tau}|$ is insignificant for all values of energies, but for some choice of energies, it becomes prominent as the baseline increases. This prominence can be visualized as a series of peaks in the plot. As the baseline increases, these peaks show the following tendencies: a shift toward the

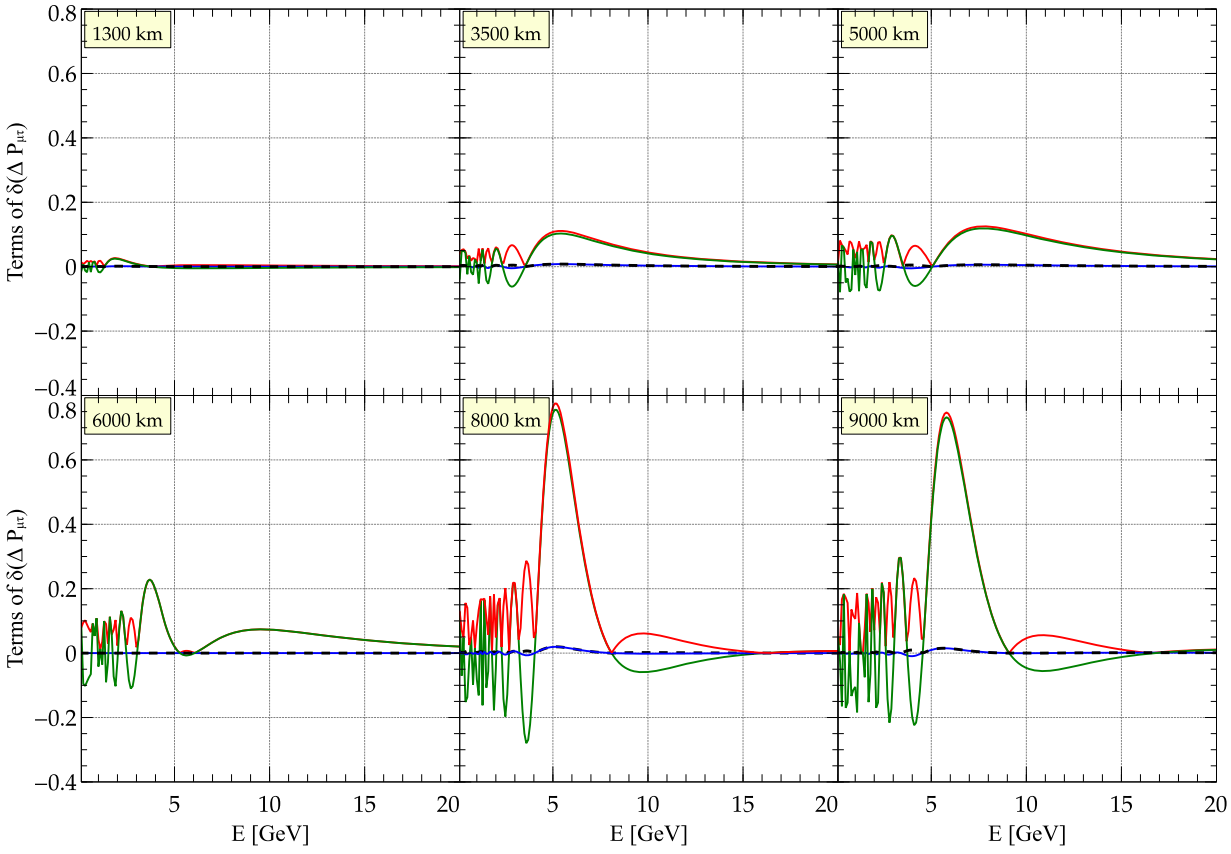

FIG. 13. $\delta(\Delta P^{CP}_{\mu\tau})$ as a function of E (GeV) for six fixed values of the baseline L (km). The dark green (blue) curve corresponds to the first (second term) of Eq. (B5). The red curve is the value of $|\delta\Delta P^{CP}_{\mu\tau}|$ in Eq. (B5). The black dashed curve corresponds to the value of $|\delta\Delta P^{CP}_{\mu\tau}|$ in the SI case.

right, becoming broad or narrow, and a change in prominence (amplitude) among the different peaks. There are two prominent long dark orangeish stretches in Fig. 6: one around $E \sim 3.5-7.5$ GeV and $L \sim 1000-5000$ km and another thinner one around $E \sim 2.5-3.5$ GeV and $L \sim 1000-5000$ km. These can be explained from the first (rightmost) peak in Fig. 13. The slant of these stretches is due to the shift in the peak position toward the right as the baseline increases. The *sharpness* of the second peak of Fig. 13 and its relatively mild shift from ∼3 to ∼6 GeV as L increases from ∼3500 to ∼9000 km produces the less-slanted thin dark stretch in Fig. 6. In addition, there are two dark patches at very long baselines in Fig. 6 around $E \sim 3-5$ GeV and $L \sim 8000-10,000$ km. The sudden rise in magnitude of the second peak at around $\gtrsim$8000 km produces the two dark spots in Fig. 6 at longer baseline values.

(iii) The features in Fig. 14 are grossly similar to Fig. 13.

The peaks can be mapped to the dark patches/regions in the NSI plot (middle row and middle panel) of Fig. 7.

(iv) We note that there are more white spaces in the middle panel of Fig. 13 than in Fig. 14. Because of the overall $\sin\lambda L/2$ dependence, the first term of $\delta(\Delta P^{CP}_{\mu\tau})$ [dark green curves in Fig. 13 and Eq. (B5)] vanishes if $\lambda L/2 \sim \pi$ or $L/E \sim 1000$ km/GeV. No such overall $\sin\lambda L/2$ is present in the first term of Eq. (B6) for $\delta(\Delta P^{CP}_{\mu\mu})$, making its vanishing less probable.

(v) The much smaller dark patches at energies $\lesssim$2 GeV in the middle panels of Figs. 6 and 7 arise because of rapid oscillation at lower energies ($\lesssim$2 GeV) in Figs. 13 and 14, respectively.

(vi) In the presence of SI only (black dashed curves in Figs. 13 and 14), we note that the values of $\delta(\Delta P^{CP}_{\mu\tau})$ and $\delta(\Delta P^{CP}_{\mu\mu})$ are very small. This explains the almost completely white/light yellowish oscillograms in Figs. 6 and 7, respectively (middle row, left column).

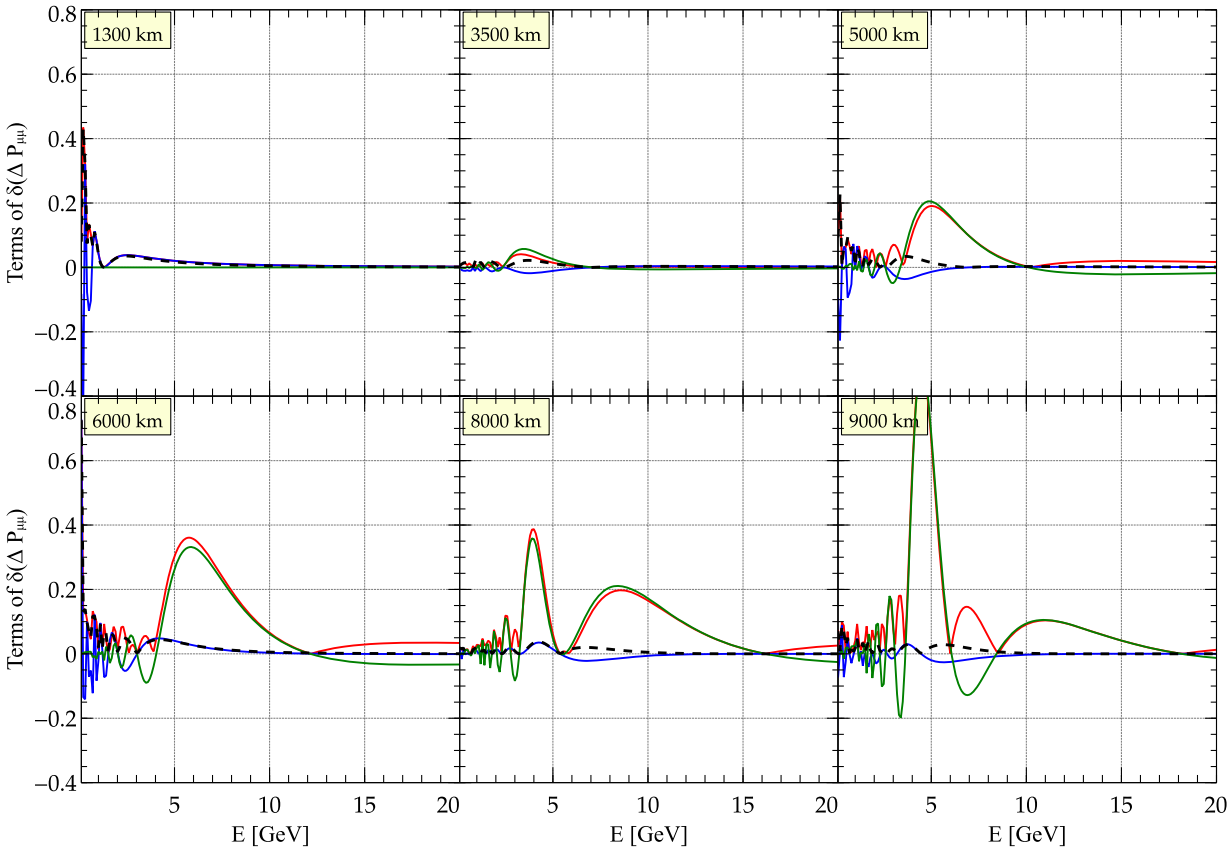

FIG. 14. $\delta(\Delta P^{CP}_{\mu\mu})$ as a function of E (GeV) for six fixed values of the baseline L (km). The dark green (blue) curve corresponds to the first (second term) of Eq. (B6). The red curve is the value of $|\delta\Delta P^{CP}_{\mu\mu}|$ in Eq. (B6). The black dashed curve corresponds to the value of $|\delta\Delta P^{CP}_{\mu\mu}|$ in the SI case.

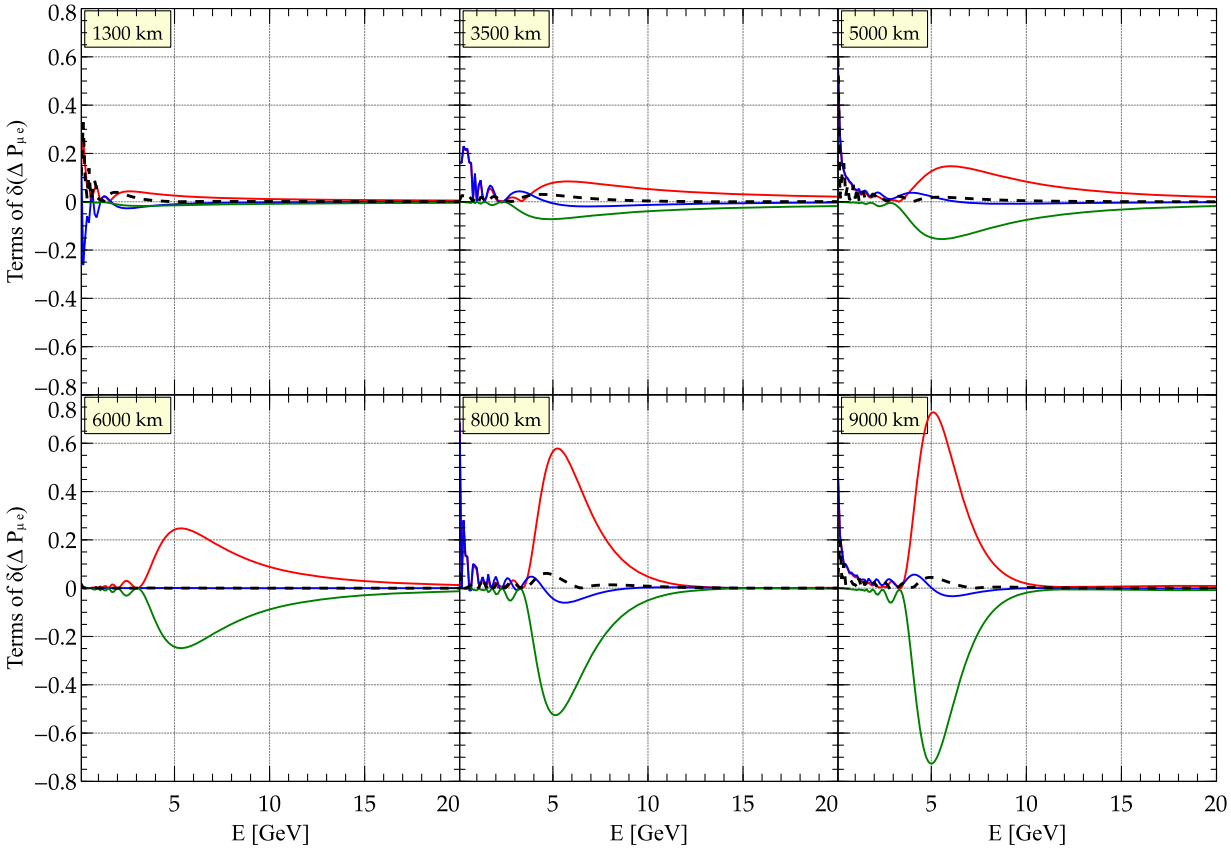

FIG. 15. $\delta(\Delta P^{CP}_{\mu e})$ as a function of E (GeV) for six fixed values of the baseline L (km). The dark green (blue) curve corresponds to the first (second term) of Eq. (B7). The red curve is the value of $|\delta\Delta P^{CP}_{\mu e}|$ in Eq. (B7). The black dashed curve corresponds to the value of $|\delta\Delta P^{CP}_{\mu e}|$ in the SI case.

2. $\mu - e$ sector

$$\begin{aligned}
\delta\Delta P^{CP}_{\mu e} &= \delta(P_{\mu e} - \bar{P}_{\mu e}) \\
&= (P_{\mu e} - \bar{P}_{\mu e})|_{\delta_{13}=\pi/2} - (P_{\mu e} - \bar{P}_{\mu e})|_{\delta_{13}=0} \\
&\approx -2\sqrt{2}Cs_{13}\left[\frac{\sin^2((1-\hat{r_A})\lambda L/2)}{(1-\hat{r_A})^2} + \frac{\sin^2((1+\hat{r_A})\lambda L/2)}{(1+\hat{r_A})^2}\right] \\
&\quad + \frac{2r_\lambda \sin 2\theta_{12}\sin(\hat{r_A}\lambda L/2)}{\hat{r_A}}\left[CD_1\cos\lambda L/2 - s_{13}D_2\sin\lambda L/2\right. \\
&\quad \left. - \frac{\sin((1-\hat{r_A})\lambda L/2)}{1-\hat{r_A}}(C+s_{13})\cos(\omega-\lambda L/2) + \frac{\sin((1+\hat{r_A})\lambda L/2)}{1+\hat{r_A}}(s_{13}-C)\cos(\omega+\lambda L/2)\right]. \qquad \text{(B7)}
\end{aligned}$$

We make the following observations from Fig. 15, which are useful for understanding the features in Fig. 6 (top row, middle panel):

(i) In Fig. 15, we plot $\delta(\Delta P^{CP}_{\mu e})$ as a function of E for different baselines. The overall behavior is dominated by the first term of Eq. (B7).

(ii) Unlike the case of $\delta(\Delta P^{CP}_{\mu\tau})$ or $\delta(\Delta P^{CP}_{\mu\mu})$, here, we have only one primary peak in Fig. 15. This peak starts appearing roughly at $L \gtrsim 5000$ km and rapidly grows with the baseline. This gives rise to the dark inverted triangular shaped patch in Fig. 6 (top row, middle column) at $E \approx 4-6$ GeV.

(iii) The orangeish blob in the same panel of Fig. 6 (at $L \lesssim 2000$ km and roughly at 5 GeV $< E <$ 9 GeV) is due to the presence of ε_{ee}[8].

[8]We have checked this numerically by assuming only the presence of the parameter ε_{ee}.

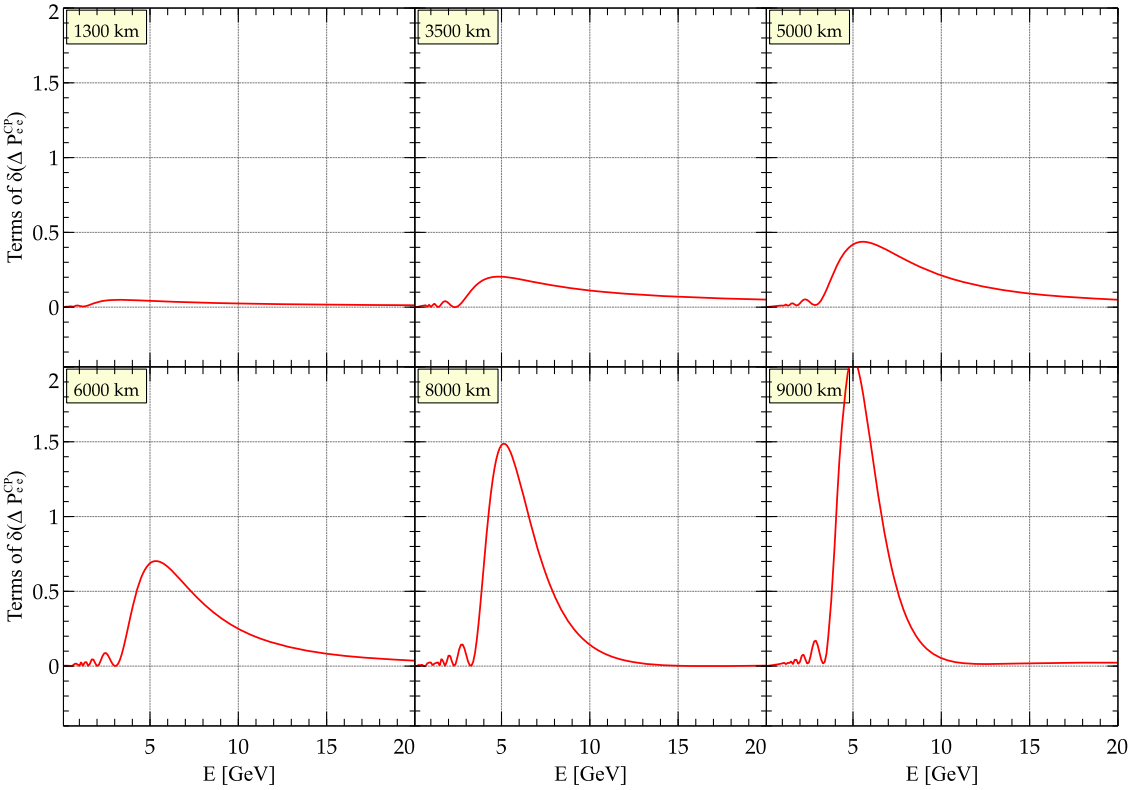

FIG. 16. $|\delta(\Delta P_{ee}^{CP})|$ as a function of E (GeV) for six fixed values of the baseline L (km). The single term in Eq. (B8) has been plotted as red curves.

3. $e-e$ sector

$$\delta\Delta P_{ee}^{CP} = \delta(P_{ee} - \bar{P}_{ee}) = (P_{ee} - \bar{P}_{ee})|_{\delta_{13}=\pi/2} - (P_{ee} - \bar{P}_{ee})|_{\delta_{13}=0} \approx 8Cs_{13}\left[\frac{\sin^2((1-\hat{r_A})\lambda L/2)}{(1-\hat{r_A})^2} + \frac{\sin^2((1+\hat{r_A})\lambda L/2)}{(1+\hat{r_A})^2}\right]. \tag{B8}$$

From Eq. (B8), we note that $\delta\Delta P_{ee}^{CP}$ contains only one term which is the same as the first term of Eq. (B7) for $\delta\Delta P_{\mu e}^{CP}$ apart from a scaling factor. In Fig. 16, we plot $\delta(\Delta P_{\mu e}^{CP})$ as a function of E for different baselines. The overall behavior is given by Eq. (B8). We note that $\delta\Delta P_{ee}^{CP}$ vanishes completely in the absence of NSI. Indeed, we see that the top left panel of Fig. 7 is completely white. Also, the second column of the top row of Fig. 7 is qualitatively similar[9] to the corresponding oscillogram for $\delta\Delta P_{\mu e}^{CP}$ (top row, second column of Fig. 6).

APPENDIX C: PATTERN OF *CP* AND *T* OSCILLOGRAMS IN THE STERILE NEUTRINO CASE

In Fig. 17, we plot the various probability differences (see the legend) that go in the calculation of $\delta\Delta P_{\alpha\beta}^{CP}$ in the presence of a sterile neutrino for the channels $\nu_\mu \to \nu_e$, $\nu_\mu \to \nu_\tau$, and $\nu_e \to \nu_\tau$ (corresponding to the three rows of Fig. 6). The baseline is taken to be 1300 km. These three panels correspond to the three rows of the right column of Fig. 6. One can see that $\delta\Delta P_{\mu\tau}^{CP}$ (represented by the red curve in Fig. 17) is quite smooth, unlike $\delta\Delta P_{\mu e}^{CP}$ or $\delta\Delta P_{e\tau}^{CP}$ that shows rapidly oscillating nature.[10] We also note that the amplitude of the wiggles is larger in the $\nu_e \to \nu_\tau$ channel than in the $\nu_\mu \to \nu_e$ channel. Indeed, in Fig. 6 (the three rows in the right column), we see that the oscillogram is mostly *smooth* in the $\nu_\mu \to \nu_\tau$ channel. Also, the $\nu_e \to \nu_\tau$ channel seems to be more *wiggly* than the $\nu_\mu \to \nu_e$ channel in the oscillogram.[11]

[9]The numerical factor $2\sqrt{2}$ makes the dark patches in the oscillogram for $\delta\Delta P_{ee}^{CP}$ only darker.

[10]These rapid secondary oscillations are the manifestations of a high $\Delta m_{41}^2 \sim 1$ eV^2.

[11]Note from Table III that we have considered a value of 15° for θ_{34}, which is quite large compared to θ_{14} (~8°) and θ_{24} (~5°). The large allowed range for θ_{34} (< 25°) permits us to use such a large value for it. Although θ_{34} has a marginal effect on the $\nu_\mu \to \nu_e$ channel, the $\nu_e \to \nu_\tau$ channel depends quite significantly on θ_{34}. This, in turn, produces the large wiggles for $\delta\Delta P_{e\tau}^{CP}$.

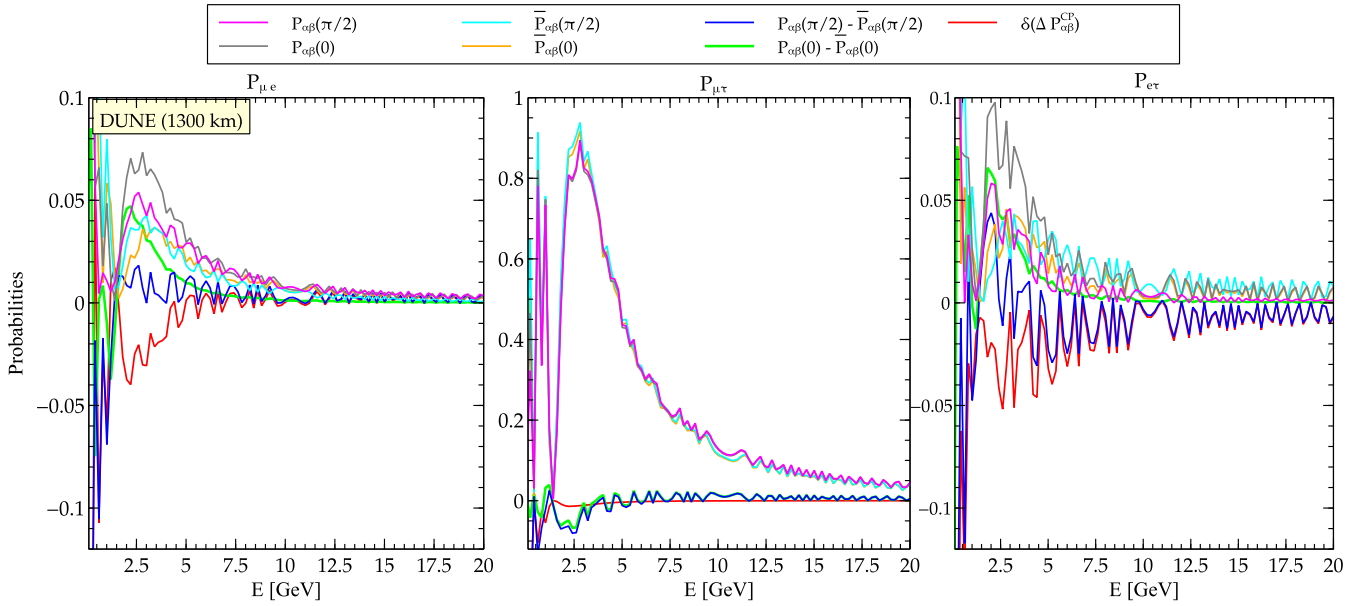

FIG. 17. Probability differences for the appearance channels in the sterile neutrino case and size of the wiggles for different channels for a fixed baseline of 1300 km.

[1] B. Pontecorvo, Sov. Phys. JETP **26**, 984 (1968).
[2] T. Kajita and A. B. McDonald, Nobel Prize in Physics in 2015.
[3] F. Capozzi, G. L. Fogli, E. Lisi, A. Marrone, D. Montanino, and A. Palazzo, Phys. Rev. D **89**, 093018 (2014).
[4] D. V. Forero, M. Tórtola, and J. W. F. Valle, Phys. Rev. D **90**, 093006 (2014).
[5] I. Esteban, M. C. Gonzalez-Garcia, M. Maltoni, I. Martinez-Soler, and T. Schwetz, J. High Energy Phys. 01 (2017) 087.
[6] J. Beringer *et al.* (Particle Data Group Collaboration), Phys. Rev. D **86**, 010001 (2012).
[7] S. Parke and M. Ross-Lonergan, Phys. Rev. D **93**, 113009 (2016).
[8] Y. Farzan and A. Yu. Smirnov, Phys. Rev. D **65**, 113001 (2002).
[9] M. Kobayashi and T. Maskawa, Prog. Theor. Phys. **49**, 652 (1973).
[10] J. Arafune, M. Koike, and J. Sato, Phys. Rev. D **56**, 3093 (1997); **60**, 119905(E) (1999).
[11] S. M. Bilenky, C. Giunti, and W. Grimus, Phys. Rev. D **58**, 033001 (1998).
[12] J. Burguet-Castell, M. B. Gavela, J. J. Gomez-Cadenas, P. Hernandez, and O. Mena, Nucl. Phys. **B608**, 301 (2001).
[13] H. Nunokawa, S. J. Parke, and J. W. F. Valle, Prog. Part. Nucl. Phys. **60**, 338 (2008).
[14] G. C. Branco, R. G. Felipe, and F. R. Joaquim, Rev. Mod. Phys. **84**, 515 (2012).
[15] T. Ohlsson, H. Zhang, and S. Zhou, Phys. Rev. D **87**, 053006 (2013).
[16] H. Minakata and H. Nunokawa, Phys. Lett. B **495**, 369 (2000).
[17] M. Masud, A. Chatterjee, and P. Mehta, J. Phys. G **43**, 095005 (2016).
[18] A. de Gouvêa and K. J. Kelly, Nucl. Phys. **B908**, 318 (2016).
[19] P. Coloma, J. High Energy Phys. 03 (2016) 016.
[20] M. Masud and P. Mehta, Phys. Rev. D **94**, 013014 (2016).
[21] M. Masud and P. Mehta, Phys. Rev. D **94**, 053007 (2016).
[22] M. Blennow, S. Choubey, T. Ohlsson, D. Pramanik, and S. K. Raut, J. High Energy Phys. 08 (2016) 090.
[23] D. V. Forero and P. Huber, Phys. Rev. Lett. **117**, 031801 (2016).
[24] A. de Gouvêa and K. J. Kelly, arXiv:1605.09376.
[25] S. Fukasawa, M. Ghosh, and O. Yasuda, Phys Rev. D **95**, 055005 (2017).
[26] J. Liao, D. Marfatia, and K. Whisnant, J. High Energy Phys. 01 (2017) 071.
[27] R. Gandhi, B. Kayser, M. Masud, and S. Prakash, J. High Energy Phys. 11 (2015) 039.
[28] S. K. Agarwalla, S. S. Chatterjee, A. Dasgupta, and A. Palazzo, J. High Energy Phys. 02 (2016) 111.
[29] S. K. Agarwalla, S. S. Chatterjee, and A. Palazzo, J. High Energy Phys. 09 (2016) 016.
[30] S. Choubey and D. Pramanik, Phys. Lett. B **764**, 135 (2017).
[31] D. Dutta, R. Gandhi, B. Kayser, M. Masud, and S. Prakash, J. High Energy Phys. 11 (2016) 122.
[32] S. K. Agarwalla, S. S. Chatterjee, and A. Palazzo, Phys. Rev. Lett. **118**, 031804 (2017).

[33] M. Blennow, P. Coloma, E. Fernàndez-Martìnez, J. Hernandez-Garcia, and J. Lopez-Pavon, arXiv:1609.08637.
[34] K. N. Deepthi, S. Goswami, and N. Nath, arXiv:1612.00784.
[35] S.-F. Ge, P. Pasquini, M. Tórtola, and J. W. F. Valle, Phys. Rev. D **95**, 033005 (2017).
[36] D. Dutta and P. Ghoshal, J. High Energy Phys. 09 (2016) 110.
[37] O. G. Miranda, M. Tórtola, and J. W. F. Valle, Phys. Rev. Lett. **117**, 061804 (2016).
[38] F. J. Escrihuela, D. V. Forero, O. G. Miranda, M. Tórtola, and J. W. F. Valle, arXiv:1612.07377.
[39] C. S. Fong, H. Minakata, and H. Nunokawa, J. High Energy Phys. 02 (2017) 114.
[40] E. K. Akhmedov, Phys. Scr. **T121**, 65 (2005).
[41] E. K. Akhmedov, P. Huber, M. Lindner, and T. Ohlsson, Nucl. Phys. **B608**, 394 (2001).
[42] Z.-z. Xing, Phys. Rev. D **88**, 017301 (2013).
[43] P. I. Krastev and S. T. Petcov, Phys. Lett. B **205**, 84 (1988).
[44] S. Toshev, Mod. Phys. Lett. A **06**, 455 (1991).
[45] P. Mehta, Phys. Rev. D **79**, 096013 (2009).
[46] P. Mehta, arXiv:0907.0562.
[47] Y. Farzan and A. Yu. Smirnov, J. High Energy Phys. 01 (2007) 059.
[48] M. Yu. Khlopov and S. T. Petcov, Phys. Lett. **99B**, 117 (1981).
[49] Z.-z. Xing, Phys. Lett. B **487**, 327 (2000).
[50] S. Antusch, J. P. Baumann, and E. Fernàndez-Martìnez, Nucl. Phys. **B810**, 369 (2009).
[51] Y. Farzan, Phys. Lett. B **748**, 311 (2015).
[52] Y. Farzan and I. M. Shoemaker, J. High Energy Phys. 07 (2016) 033.
[53] D. V. Forero and W.-C. Huang, J. High Energy Phys. 03 (2017) 018.
[54] C. Biggio, M. Blennow, and E. Fernandez-Martinez, J. High Energy Phys. 08 (2009) 090.
[55] S. Davidson, C. Pena-Garay, N. Rius, and A. Santamaria, J. High Energy Phys. 03 (2003) 011.
[56] M. C. Gonzalez-Garcia and M. Maltoni, J. High Energy Phys. 09 (2013) 152.
[57] F. P. An *et al.* (Daya Bay Collaboration), Phys. Rev. Lett. **113**, 141802 (2014).
[58] B. Jones, in talk at FermiLab, Batavia IL 60510-5011, 2016 (unpublished), https://hep.uchicago.edu/seminars/semwin2016/BenJones1.pdf.
[59] P. Adamson *et al.* (MINOS Collaboration), Phys. Rev. Lett. **107**, 011802 (2011).
[60] J. Kopp, P. A. N. Machado, M. Maltoni, and T. Schwetz, J. High Energy Phys. 05 (2013) 050.
[61] G. H. Collin, C. A. Argüelles, J. M. Conrad, and M. H. Shaevitz, Phys. Rev. Lett. **117**, 221801 (2016).
[62] W. Marciano and Z. Parsa, Nucl. Phys. B, Proc. Suppl. **221**, 166 (2011).
[63] V. D. Barger, K. Whisnant, S. Pakvasa, and R. J. N. Phillips, Phys. Rev. D **22**, 2718 (1980).
[64] E. K. Akhmedov, R. Johansson, M. Lindner, T. Ohlsson, and T. Schwetz, J. High Energy Phys. 04 (2004) 078.
[65] T. Kikuchi, H. Minakata, and S. Uchinami, J. High Energy Phys. 03 (2009) 114.
[66] K. Asano and H. Minakata, J. High Energy Phys. 06 (2011) 022.
[67] J. Liao, D. Marfatia, and K. Whisnant, Phys. Rev. D **93**, 093016 (2016).